JGR Solid Earth

RESEARCH ARTICLE
10.1029/2025JB031803

Magma Storage Below Sabancaya Volcano (Southern Peru) Imaged by Broadband Magnetotellurics

Jose-Luis Torres[1,2,3], Svetlana Byrdina[2], Gonzalo Romero-Beltran[1], Stéphane Garambois[2], Volker Rath[4], Yanet Antayhua[1], Marco Rivera[1], Alain Burgisser[2], Roger Machacca[1], Marco Milla[3], Hernando Tavera[1], and Philip Hering[5,6]

[1]Instituto Geofísico del Perú, Lima, Perú, [2]University Grenoble Alpes, University Savoie Mont Blanc, CNRS, IRD, University G. Eiffel, ISTerre, Grenoble, France, [3]Pontificia Universidad Católica del Perú, Lima, Perú, [4]Dublin Institute for Advanced Studies, Dublin, Ireland, [5]Goethe-University Frankfurt, Institute for Geoscience, Applied Geophysics, Frankfurt, Germany, [6]Institute for Geothermal Research Management, Bingen, Germany

Abstract Sabancaya volcano is one of the most active volcanoes in the Central Andes. Its ongoing eruptive process is accompanied by large-scale deformation, with activation of the Huambo-Cabanaconde fault system, marked by intense seismicity over an area of about 50 × 30 km^2. We present a pilot magnetotelluric survey performed in 2022, covering the Ampato-Sabancaya complex, Hualca-Hualca volcano, as well as the related system of normal faults. Our three-dimensional electrical resistivity model reveals pronounced vertical gradients and lateral contrasts at elevations above sea level, along with generally low resistivity values at depth. Seismicity at depths >4 km below sea level predominantly occurs in a low resistivity environment: 90% of seismic events occur at resistivity values below 10 Ωm. Two prominent electrical conductors (<0.5 and 2–4 Ωm) are imaged at depths 11–18 km and 3–8 km, respectively. Using petrological constraints, we interpret them as the signature of the magmatic plumbing system, connecting the Hualca-Hualca and Ampato-Sabancaya volcanoes. The deeper conductor is inferred to represent a magma reservoir situated beneath the older Hualca-Hualca volcano, consistent with long-term deformation and seismicity. It is connected to the laterally offset shallow magma chamber below Sabancaya. At depth 2–10 km, a strong conductor (<0.1 Ωm) is imaged in the Huambo-Cabanaconde fault zone. The extremely high conductivity of this body is attributed to the abundance of ultra-saline brines, originating from the deep magma reservoir below. We speculate that the strong seismicity cluster detected in 2013 facilitated the passage of magmatic fluids exsolved from the magma reservoir, and replenished this ultra-conductive body.

Plain Language Summary Sabancaya volcano is one of the most active volcanoes in the Central Andes. Its ongoing eruptions are accompanied by diverse activity across an area much larger than the volcanic edifice, including strong earthquakes throughout the wider Colca region, and especially near a fault system close to the Huambo–Cabanaconde area, more than 20 km from the volcano. In addition, large-scale deformation affects the area centered on the older, dormant Hualca-Hualca volcano, about 10 km from Sabancaya. The goal of this study is to image the magmatic plumbing system to better understand the eruptive history and the processes driving this large-scale unrest. To do so, we use magnetotellurics, a passive geophysical imaging method that measures subsurface electrical resistivity. The method is sensitive to fluids, including aqueous fluids and magma, which allows us to propose a model of the crustal fluid distribution. We delineate the geometry of the magma-feeding system beneath Hualca-Hualca, which appears connected to a shallow magma chamber directly beneath Sabancaya. Above this magmatic system, at shallow depth, we image a hydrothermal system.

Key Points:

- First comprehensive magnetotelluric survey of the high-risk Sabancaya volcano, providing new insights on key internal structures
- A conceptual model for the plumbing system is derived from a 3D resistivity model, petrophysical constraints, and seismicity distribution
- Magma reservoir is imaged beneath the center of large-scale deformation, laterally offset from the currently erupting Sabancaya volcano

Supporting Information:

Supporting Information may be found in the online version of this article.

Correspondence to:

S. Byrdina,
svetlana.byrdina@univ-smb.fr

Citation:

Torres, J.-L., Byrdina, S., Romero-Beltran, G., Garambois, S., Rath, V., Antayhua, Y., et al. (2026). Magma storage below Sabancaya volcano (southern Peru) imaged by broadband magnetotellurics. *Journal of Geophysical Research: Solid Earth*, *131*, e2025JB031803. https://doi.org/10.1029/2025JB031803

Received 15 APR 2025
Accepted 2 FEB 2026
Corrected 2 MAR 2026

This article was corrected on 2 MAR 2026. See the end of the full text for details.

Author Contributions:

Conceptualization: Jose-Luis Torres, Svetlana Byrdina, Yanet Antayhua, Hernando Tavera
Data curation: Jose-Luis Torres, Svetlana Byrdina, Gonzalo Romero-Beltran
Formal analysis: Jose-Luis Torres, Svetlana Byrdina, Volker Rath, Philip Hering

1. Introduction

Enhancing our knowledge of magmatic systems beneath active volcanoes will help designing volcanic monitoring, anticipate risk associated with volcanic eruptions, and improve the management of volcanic hazards (Becerril et al., 2013; Chaussard & Amelung, 2014; Dong et al., 2023; Edmonds & Woods, 2018). The physical and chemical processes occurring within a volcanic complex, where partial melt, hydrothermal systems, and magmatic fluids coexist, control the timing, style, and magnitude of a volcanic eruption (Burchardt, 2018). Moreover, the location of magma reservoirs and exsolved saline fluids is of economic interest due to their potential for exploitation of geothermal energy and mineral resources (Blundy et al., 2021; Reinsch et al., 2017; Watanabe et al., 2022).

Funding acquisition: Svetlana Byrdina, Stéphane Garambois, Yanet Antayhua, Hernando Tavera
Methodology: Marco Rivera, Alain Burgisser
Supervision: Svetlana Byrdina, Stéphane Garambois, Marco Milla
Writing – original draft: Jose-Luis Torres
Writing – review & editing: Jose-Luis Torres, Svetlana Byrdina, Stéphane Garambois, Volker Rath, Marco Rivera, Alain Burgisser, Roger Machacca, Marco Milla

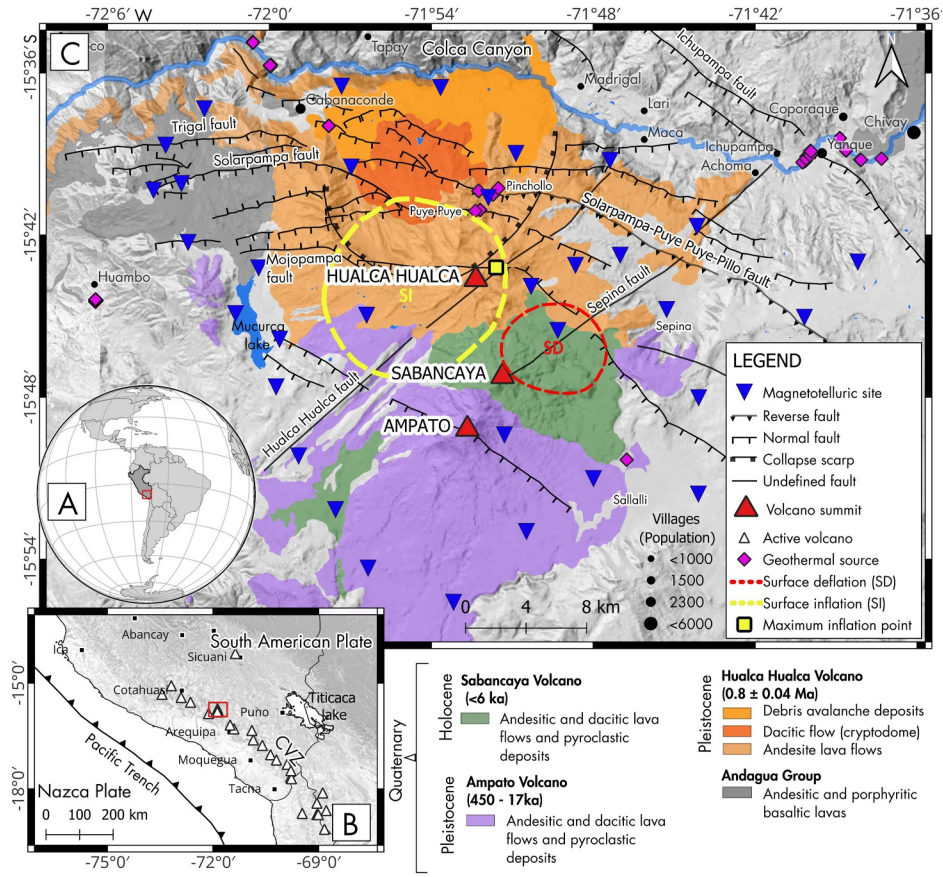

Figure 1. Simplified geological and structural maps of the Ampato-Sabancaya complex and the Hualca-Hualca volcano: (a, b) show the location of Sabancaya volcano and the study area, marked with a red rectangle, situated at the northern end of the Central Volcanic Zone (CVZ) of the Andes in southern Peru. Red triangles indicate the summits of the three volcanoes mentioned in this study. (c) The orange tones represent Pleistocene andesitic lava flows associated with the ancient Hualca-Hualca volcano, on which the Ampato edifice developed. The green color corresponds to the sequences of dacitic and andesitic lavas of the Sabancaya edifice, overlaying the Ampato sequences. Faults are marked by black lines, and geothermal manifestations such as thermal springs are shown as magenta rhombus symbols. The underlying information (geology, faults, and geothermal features) was obtained from the GEOCATMIN system of INGEMMET https://geocatmin.ingemmet.gob.pe/. Blue inverted triangles indicate magnetotelluric sites, while black circles of varying size represent the population living along the Colca Canyon. The yellow dashed lines delimit the approximate zone of surface inflation (SI) and yellow square the maximum inflation, which occurred between 2013 and 2019 (MacQueen et al., 2020), while the red dashed line marks a zone of surface deflation (SD) between January 2012 and May 2013 (Jay et al., 2015).

Sabancaya volcano is located within the province of Caylloma, 70–75 km northwest of the city of Arequipa, the second most populated city in Peru (Figure 1b), 15° 49.3′S; 71° 52.7′W, and reaches an elevation of 5,980 m above sea level (m a.s.l.). It is considered the second most active volcano in Peru after Ubinas (Rivera et al., 2023). Sabancaya is usually assigned to the active Ampato-Sabancaya volcanic complex, and together with its neighbor, dormant Hualca-Hualca volcano, belongs to the Central Volcanic Zone (CVZ) of the Andes. It is the youngest of the three mentioned volcanoes (Samaniego et al., 2016).

Geodetic studies suggest the presence of a magma reservoir located at ≈13 km depth beneath the Hualca-Hualca volcano (Boixart et al., 2020; MacQueen et al., 2020). This deep magmatic reservoir is thought to feed and interact with a shallower magma chamber at ≈6 km depth located beneath Sabancaya (Gerbe & Thouret, 2004). In addition, preliminary studies using the Self-Potential method provide evidence of a hydrothermal system beneath the Ampato and Sabancaya volcanoes (Alvarez, 2017; Puma et al., 2018). Geochemical and seismic studies suggest this hydrothermal system extends beneath Hualca-Hualca as well, manifesting at the surface through sulfate-rich hot springs (e.g., Pinchollo and Puye Puye geysers), many of which are located along active fault systems characterized by intense seismicity (Machacca et al., 2023; Tyc et al., 2022). However, these studies do

not provide the geometry of the magma reservoir and conduits through which the magma ascends, making it difficult to understand the origin of the seismicity pattern and the relationship between tectonic and volcanic activity. For this reason, we performed a broadband magnetotelluric survey to characterize the geometry of the plumbing system below this volcanic complex, encompassing also a system of adjacent normal faults reactivated in the pre-eruptive phase of the latest episode (since 2013).

In active volcanic regions, numerous studies have employed multidisciplinary approaches to investigate the structure and dynamics of magmatic and hydrothermal systems. Díaz et al. (2020) and Heise et al. (2024) have correlated seismicity and magnetotelluric (MT) results, surface deformation, and petrology to investigate the interactions between magmatic and tectonic processes. MT studies of Chilean volcanoes such as Villarrica (Pavez et al., 2020) and Osorno (Díaz et al., 2020), have allowed for the delineation of the distribution of magmatic bodies and hydrothermal systems, providing a detailed view of magma ascent mechanisms and the activation of crustal faults. Moreover, studies on volcanoes such as Fogo in Azores Islands (Hogg et al., 2024) and Long Valley Caldera in the United States (Peacock et al., 2016) have shown how the integration of MT data with seismicity and surface deformation significantly enhances the understanding of magmatic systems in volcanic environments.

The MT method is a passive geophysical technique, that measures simultaneously the variations of the electric and magnetic field at the Earth's surface (Cagniard, 1953; Tikhonov, 1950), and allows determining the electrical resistivity from a few tens of meters to several hundreds of kilometers of depth (Simpson & Bahr, 2005). Electrical resistivity is sensitive to the presence of fluids, temperature, rock alteration, and partial melt at greater depths. Therefore, magnetotellurics is a well adapted tool to image hydrothermal and magmatic reservoirs. Under certain conditions, it will allow estimating the fraction of magma in these reservoirs (e.g., Comeau et al., 2016; Cordell et al., 2018; Hanneson & Unsworth, 2023; Jenkins et al., 2023; Wawrzyniak et al., 2025). This study aims to advance our understanding of the structures beneath the Sabancaya volcano, offering new insights into the hydrothermal system and the geometry of both shallow and deep magmatic reservoirs. In this paper, we analyze data from 33 magnetotelluric soundings distributed around the Sabancaya, Ampato, and Hualca-Hualca volcanoes (Figure 1c). This enables us to obtain, for the first time, a three-dimensional crustal resistivity model of this volcanic complex. The resistivity model, obtained using the ModEM code (Kelbert et al., 2014), will be discussed in the light of seismic, geodetic, and petrological data (e.g., Boixart et al., 2020; Machacca et al., 2023; MacQueen et al., 2020; Rivera et al., 2023). In particular, the correlation of seismicity patterns with the resistivity model provides critical insights into the nature of seismic sources. We also compare our 3-D resistivity model to geodetic models of the magmatic sources responsible for surface deformation (MacQueen et al., 2020). In a second step, we estimate the range of possible partial melt fractions based on laboratory electrical resistivity values of hydrous andesitic melts (Laumonier et al., 2017) using modified Archie's law (Glover et al., 2000), and we then compare these estimates with recent petrological constraints derived from the latest eruptive products.

2. Geology of Sabancaya Volcano and Magma Composition

The Sabancaya volcano belongs to a region composed of Mesozoic and Cenozoic volcanic and sedimentary formations (Sebrier & Soler, 1991). To the north, the Ampato-Sabancaya complex borders the Hualca-Hualca (6,025 m a.s.l.), an ancient and highly eroded volcanic edifice. Its lavas emplaced on Pliocene ignimbrites form the basis of the current volcanic complex. Dating by Gerbe and Thouret (2004) yielded an age of 0.80±0.04 Ma for the andesitic lava flow of Hualca-Hualca. To the south, the Ampato stratovolcano (6,280 m a.s.l.) developed and experienced several eruptive phases during the Upper Pleistocene to Holocene period (Rivera et al., 2016; Samaniego et al., 2016). Dacitic lava flows from the upper part of the Ampato cone have been dated to 17±6 ka (Samaniego et al., 2016).

In this paragraph we follow Rivera et al. (2016) and Samaniego et al. (2016) to give a short outline of the evolution of the volcanic complex. Sabancaya has been active since the early Holocene (≈6 ka). Its chronological development consists of a sequence of dacitic and andesitic lava flows, along with pyroclastic deposits, and began after volcanic activity had ceased at the neighboring Ampato volcano. The main evolution of Ampato occurred in two stages during the Middle Pleistocene (≈450 to 400 ka, and 230 to 200 ka), followed by effusive activity between 80 and 70 ka. With an eruptive rate of 0.6–1.7 km^3/ka, significantly higher than that of Ampato (≈0.1 km^3/ka), Sabancaya represents a highly active volcanic system.

During its evolution, Sabancaya has emitted andesitic to dacitic lavas (58.2–65.7 wt% SiO_2) with a medium to high-K calc-alkaline affinity, high concentrations of LILE (K, Rb, Ba, Th), and low concentrations of HFSE (Nb, Zr) and HREE (Yb) (Rivera et al., 2023). These characteristics indicate that mantle-derived magmas have been significantly affected by assimilation processes during their evolution (Rivera et al., 2023), due to the thick (65–70 km) continental crust beneath the Central Volcanic Zone (CVZ) in southern Peru (Beck et al., 1996).

Over the last 500 years, Sabancaya's activity has been dominated by mild to moderate explosive eruptions with a Volcanic Explosivity Index (VEI) ranging from 1 to 3 (Huamán, 1995; Samaniego et al., 2016; Siebert et al., 2011; Thouret et al., 1994). The most recent eruption of Sabancaya volcano, which lasted from 1990 to 1998, reached a VEI of 3 (Siebert et al., 2011) and was characterized by Vulcanian explosions and sustained ash emissions (Gerbe & Thouret, 2004; Guillande & Throuret, 1992). The most intense phase of explosive activity occurred between May and June 1990 and involved alternating Vulcanian and phreatomagmatic events (Gerbe & Thouret, 2004). In 2013, Sabancaya entered a new eruptive phase marked by intense seismic activity (seismic activity between 2013 and 2020 is briefly characterized in the following paragraph and will be described in more detail in Section 2.3.) and persistent gas emissions. Since November 2016, the volcano has produced frequent Vulcanian explosions with ash plumes and sustained seismicity, an activity that has continued through the present (2025) (Centeno et al., 2025). This ongoing eruption is characterized by recurrent gas-and-ash explosions, with eruptive columns reaching up to 5 km above the summit (July 2017), and by episodes of lava dome growth documented between 2016 and 2020 (Rivera et al., 2023). Petrological studies indicate that the 1990–1998 eruption produced andesitic to dacitic magmas (60–64 wt% SiO_2) (Gerbe & Thouret, 2004), whereas the products of the 2017 eruption were predominantly andesitic (58.2–61.2 wt% SiO_2) (Rivera et al., 2023). Textural, mineralogical, and chemical evidence suggest that the 1990–1998 eruptions primarily produced hybrid andesites induced by magma recharge from more mafic magmas in a shallow reservoir. The crystallization pressure, estimated from amphibole phenocrysts using the "Al-in hornblende" barometer, ranges from 200 to 350 MPa, while the pre-eruptive temperature estimates for the magmas expelled during 1990–1998 are 940±50°C. Gerbe and Thouret (2004) mention that in the dacite, the stability of amphibole requires a minimum of 4.2 wt% H_2O. This water content estimation is in agreement with the water content (3 and 6 wt%) estimated for andesitic, dacitic, and rhyolitic magmas at the Ubinas volcano, located in a similar geo-tectonic setting (Samaniego et al., 2020).

After approximately 15 years of rest, an episode of volcanic unrest began in February 2013 and has continued through to the present (2025). The period 2013–2020, which is the focus of this study, was characterized by two stages of activity: a pre-eruptive stage (2013–2016) with intense seismicity and degassing (Jay et al., 2015; Machacca et al., 2023; Tavera et al., 2013), and a co-eruptive stage characterized by explosions with ash emissions accompanied by surface deformation (Machacca et al., 2023; Puma & Torres, 2020). A common feature of both periods is the occurrence of intense shallow seismic activity (hypocenters <17 km) of Volcano-Tectonic (VT) type, with magnitudes up to M4.5, and epicenters located northwest, north, northeast of Sabancaya, around Hualca-Hualca (Machacca et al., 2023). Recent seismological studies relate the intense VT-type activity to magmatic intrusions and fluid pressure changes, destabilizing faults under critical stress (Machacca et al., 2023; MacQueen et al., 2020; Puma & Torres, 2020).

2.1. Tectonic and Structural Control

Tectonic activity in the area surrounding the Colca Canyon, including the Ampato-Sabancaya complex and the Hualca-Hualca volcano, is evidenced by the presence of numerous faults and lineaments. Geological studies carried out in the Sabancaya region (Huamán, 1995; Mering et al., 1996; Sébrier et al., 1985) identified at least three active fault systems (see Figure 1c):

1. A system of normal faults, Ichupampa and Huanca, of northwest-southeast direction and strike N135°. It presents mainly vertical movements with a small sinistral component (Antayhua et al., 2002; Mering et al., 1996). On a regional scale, these faults are located within an extensional tectonic context, parallel to the Peru-Chile rift (Huaman-Rodrigo et al., 1993; Mering et al., 1996). The Ichupampa fault is located northeast of the Sabancaya volcano (Figure 1c).
2. The Huambo-Cabanaconde fault system comprising Trigal, Solarpampa and Mojopampa normal faults, with east-west direction, N85°. This system is parallel to the Colca Canyon and located to the west and southwest of the town of Cabanaconde (Figure 1c). The movement of the faults is linked to the tectonic activity that

occurred during the Holocene (Antayhua et al., 2002; Sébrier et al., 1985). The Trigal and Solarpampa faults, extending between 18 and 22 km in length, show southward displacement (Huamán, 1995; Sébrier et al., 1985).

3. The Sepina fault, with northeast-southwest direction and N50° strike, has also a vertical movement. It is located northeast of the Ampato-Sabancaya complex and Hualca-Hualca volcano, and crosses the Colca Canyon (Figure 1c) and the localities of Achoma, Yanque and Coporaque (Huaman-Rodrigo et al., 1993; Mering et al., 1996). This fault appears to be directly related to the Ampato-Sabancaya complex. Parallel to the Sepina fault is the northeast-southwest Hualca-Hualca fault, which crosses the summit of the volcano of the same name.

2.2. Surface Deformation

Previous deformation studies conducted in the Ampato-Sabancaya volcanic complex and Hualca-Hualca volcano have provided a detailed view of the magmatic and tectonic activity in the region, using advanced techniques such as DInSAR (Differential Synthetic Aperture Radar Interferometry) and GNSS (Global Navigation Satellite System). Among the most prominent studies are those by Jay et al. (2015), MacQueen et al. (2020), and Boixart et al. (2020), which analyzed the surface deformations related to the magmatic activity of Sabancaya volcano. According to Jay et al. (2015), episodes of subsidence and uplift associated with Volcano-Tectonic (VT) swarms and moderate magnitude earthquakes were identified, suggesting an interaction between magmatic and tectonic processes in the region. On the other hand, MacQueen et al. (2020) identified the area of maximum deformation between 2013 and 2019 at the summit of Hualca-Hualca, northwest of Sabancaya volcano, revealing interactions between VT earthquakes, episodic magma intrusion, and high subsurface fluid pressures in the region. Boixart et al. (2020) examined magmatic inflation and its relationship with the region's seismic dynamics, using DInSAR and GNSS data acquired between 2014 and 2019. During this period, a notably high deformation rate was observed, averaging 3–4 cm/year, particularly in the area located to the northwest of Sabancaya volcano, in the Hualca-Hualca region. The surface deformation revealed radially symmetric inflation, with the highest intensity located 7 km NNW of the main crater of Sabancaya, suggesting magma accumulation in the subsurface and its relationship with the continuous eruptive activity at Sabancaya since 2016 (Boixart et al., 2020; MacQueen et al., 2020).

These studies proposed from modeling that the magmatic intrusion, source of this surface deformation, should be located at a depth between 13 and 14 km, according to MacQueen et al. (2020), and between 12 and 15 km, according to Boixart et al. (2020), beneath the surface of Hualca-Hualca volcano. These depths were estimated using a spherical pressure source model that adjusts the geodetic observations (Boixart et al., 2020). The inversion is based on surface deformation measurements, comparing them with synthetic one generated by various magmatic intrusion models. Additionally, the location of the surface deformation coincides with a high VT seismic activity zone described by Machacca et al. (2023), located in the Hualca-Hualca region.

These results, along with the VT earthquakes, will be compared with the resistivity model obtained from our magnetotelluric studies in Section 4. For this, the deflation surfaces (SD) characterized by ≈6 cm of vertical displacement, occurring between January 2012 and May 2013 (Jay et al., 2015), 4 km northeast of Sabancaya volcano, with a diameter of approximately 7 km, will be used. Furthermore, the inflation surface (SI) of ≈20 cm, observed between 2013 and 2019, located 7 km northwest of Sabancaya, with a diameter of ≈12 km, and the maximum inflation point located near the highest point of Hualca-Hualca volcano [15°43.3′S; 71°51.60′W], will also be correlated (MacQueen et al., 2020), see Figure 1c.

2.3. Seismicity

The Volcano-Tectonic earthquake catalog analyzed in this study was compiled by the Geophysical Institute of Peru (IGP) through the National Volcanological Center (CENVUL), and spans from April 2013 to December 2020. VT earthquakes were recorded by both permanent and temporary seismic stations. In 2013, nine seismic stations operated simultaneously, whereas between 2014 and 2020, the number of operational stations ranged from three to seven (Machacca et al., 2023). Since 2019, the IGP-CENVUL has maintained up to seven real-time seismic stations dedicated to monitoring Sabancaya volcano (https://www.igp.gob.pe/servicios/centro-vulcanologico-nacional/).

Table 1
Seismic Catalogs

Parameter	Catalog	Refined catalog	Main earthquake
Time window	04/2013–12/2020	04/2013–12/2020	2013–2020
Number of events	23,160	7229	14
Location method	NonLinLoc	NonLinLoc	NA
Horizontal/vertical error (km)	≤10	≤3	NA
Magnitude (M_l)	1–5.3	1–4.5	4.5–5.9
Hypocentral depth (km b.s.l.)	17	17	≤60

The study conducted by Machacca et al. (2023) enhances the quality of the localization of VT earthquakes in the Sabancaya region by developing a one-dimensional (1D) velocity model using the Velest code (Kissling et al., 1994, 1995) and refining earthquake locations through the NonLinLoc software package (Lomax et al., 2000). As a result, a comprehensive catalog of 23,160 earthquakes was compiled, with local magnitudes (Ml) ranging from M1.0 to M5.3 and depth changes shallower than 17 km below sea level (from now on called b.s.l.). The earthquakes in the catalog present horizontal errors of ≤5 km, vertical errors of ≤10 km, and a temporal RMS < 0.35 s (see Table 1). Note that the maximum elevation of the earthquakes is 4.3 km because the top of the 1D velocity model is set to 4.3 km a.s.l., which corresponds to the mean free surface elevation of the study area (Figure 2c). A limited number of events occurred above this depth, mainly related to eruptive seismicity, such as Long-Period events, which are difficult to locate.

The large number of VT earthquakes recorded between 2013 and 2020 at Sabancaya was studied in detail through a temporal and spatial distribution analysis, as described in Machacca et al. (2023). Through its national seismic network installed throughout Peru, IGP also records major earthquakes with magnitudes ≥M4.0. During the study period in the Sabancaya region, up to 14 significant events were recorded around the region with magnitudes ranging between M4.5 and M5.9 (https://www.gob.pe/igp). Furthermore, the focal mechanisms of these events were obtained from the Global Centroid Moment Tensor Catalog (https://www.globalcmt.org/).

For the purpose of this study, the total number of earthquakes in the catalog by Machacca et al. (2023) was filtered, considering only those earthquakes with vertical and horizontal localization errors of ≤3 km (see Table 1), resulting in a refined catalog of 7229 earthquakes. This filtering allows for a more precise delineation of conductive bodies evidenced by the MT method in correlation with the depth distribution of seismicity.

In general, the refined catalog observed in the most seismically active regions shows seismic clusters embedded within a circle of radius less than 23 km, located to the northwest, north, and northeast of the Sabancaya volcano (Figures 2a and 2b). The distribution of the number of earthquakes as a function of depth (Figure 2c), suggests the earthquakes are clustered at three depth levels (referring to the sea level). Referring to the Earth surface, three clusters shown in Figure 2c are defined like follows: shallow (<3 km below the surface), intermediate (3–8 km below the surface), and deep (>8 km below the surface).

In the following, we consider separately pre-and co-eruptive seismicity. According to MacQueen et al. (2020), intense pre-eruptive activity has likely perturbed mechanical (and therefore, also electrical) properties of rocks significantly. In contrast, co-eruptive seismicity would be assumed as contemporary with the snapshot of the MT survey, and the possible evolution of the mechanical properties since the onset of eruptive process will be neglected.

During the pre-eruptive and co-eruptive stages, different studies associate intense seismic activity with magmatic intrusions and fluid pressure, which destabilize pre-existing faults subject to a state of critical stress (Machacca et al., 2023; MacQueen et al., 2020; Puma & Torres, 2020; Torres, 2014). During the pre-eruptive stage, most of the earthquakes developed in clusters at depths >8 km below the surface, are labeled deep earthquakes (Figure 2a). Their location, with respect to the Sabancaya volcano and the zone of maximum deformation, varies between 5 and 25 km in northwest and northeast directions. Four events with magnitudes between M4.5 and M5.0 were recorded in February 2013 (Tavera et al., 2013) southeast of Ampato. Their focal mechanisms indicate the activation of strike-slip faults (Machacca et al., 2023). In July 2013, a seismic cluster was recorded with a main earthquake of moment magnitude (Mw) 5.9, 15 km northwest of the Sabancaya crater. Its focal mechanism

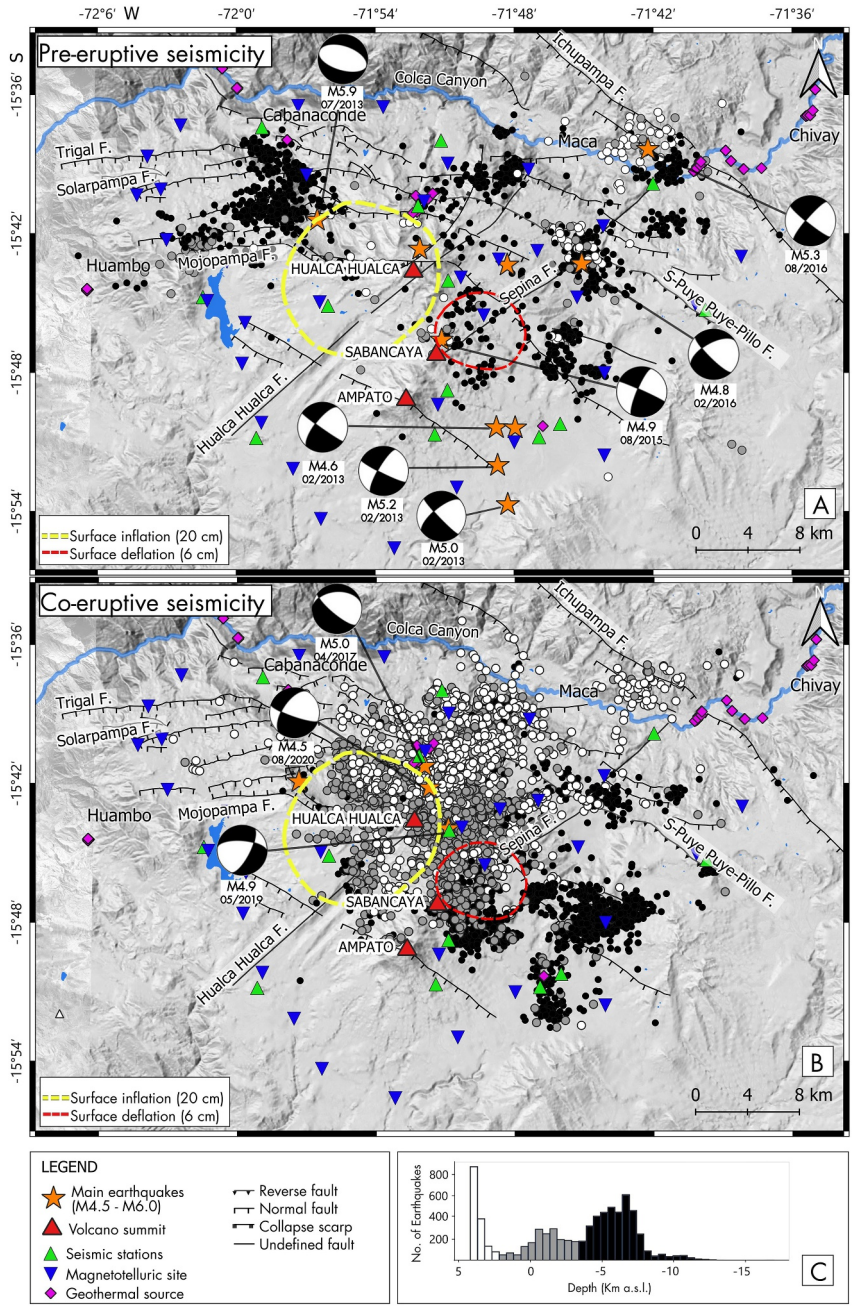

Figure 2. Seismicity 2013–2020 recorded in the Ampato-Sabancaya complex and Hualca-Hualca volcano. (a) Pre-eruptive seismicity. (b) Co-eruptive seismicity. (c) Number of earthquakes as a function of depth related to the sea level. Referring to the Earth surface, the same clusters are: shallow earthquakes in white (down to 3 km below the surface), intermediate-depth earthquakes in gray (3–8 km), and deep earthquakes in black (>8 km below the surface). The green triangles represent the permanent and temporary seismic stations used by the IGP for monitoring of the Sabancaya volcano.

corresponds to a normal fault, concordant with the Huambo-Cabanaconde normal fault system (Machacca et al., 2023; Tavera et al., 2013). Three seismic clusters were identified along the Sepina fault: the first cluster, located <5 km northeast of the Sabancaya volcano, under the zone of ground subsidence. In this zone, in August 2015, an M4.9 earthquake was recorded with a focal mechanism suggesting a strike-slip fault, concordant with the Sepina lineament. The second cluster is located about 12 km from the Sabancaya volcano, with a main earthquake of magnitude M4.8. Its focal mechanism suggests a normal fault, concordant with the Solarpampa-Puye Puye-Pilo fault, which intercepts the Sepina fault. The third cluster is located about 25 km to the northeast, at the end of

the Sepina fault, where it intersects the Ichupampa fault. The focal mechanism of the M5.3 main earthquake suggests a strike-slip fault concordant with the Sepina lineament, although it is also associated with the Ichupampa fault (Tavera et al., 2016).

During the co-eruptive stage, a predominance of shallow and intermediate earthquakes is observed to the north and northeast of the Hualca-Hualca volcano, at depths <8 km b.s.l. (Figure 2b). Most of the deep earthquakes were located northeast and southeast of the Sabancaya volcano. An important cluster of earthquakes shallower than 8 km was located northeast of the center of maximum deformation and the Hualca-Hualca fault. The focal mechanisms of the main earthquakes (M4.5, M4.9 and M5.0) are associated with normal faults, concordant with the faulting system of the area (Machacca et al., 2023).

3. Magnetotelluric Data, Processing, and Inversion

A total of 33 broadband magnetotelluric (MT) soundings were recorded in November and December 2022 around the Ampato-Sabancaya complex and Hualca-Hualca volcano, at an average distance of ≈5 km between acquisition sites (locations shown in Figure 1c), during the co-eruptive period of Sabancaya. We used Metronix Geophysics instruments, ADU-08 data logger, MSF06e coils, and nonpolarizing electrodes (Pb/PbCl2 EFP-06) forming dipoles deployed following an orthogonal arrangement in geomagnetic N-S and E-W directions. Vertical magnetic fields were only recorded at 17 sites because of digging difficulties. At each observation site, data were recorded in two separate frequency bands: the first acquisition used a 65 kHz sampling rate with a duration of 15 min, while the second acquisition employed a 256 Hz sampling rate and lasted between 20 and 40 hr. Data of two sites were disabled during processing step because of bad signal-to-noise ratio, likely due to the proximity with the electric power line.

3.1. Processing and Data Visualization

From the magnetotelluric time series data, a transformation to the frequency domain allows estimating the impedance tensor **Z** and the vertical magnetic transfer function **T**. The complex impedance tensor **Z** is defined as (Chave & Jones, 2012):

$$\begin{pmatrix} E_x \\ E_y \end{pmatrix} = \begin{pmatrix} Z_{xx} & Z_{xy} \\ Z_{yx} & Z_{yy} \end{pmatrix} \begin{pmatrix} H_x \\ H_y \end{pmatrix} \tag{1}$$

More intuitive parameters, apparent resistivity (ρ_a) and phase (ϕ), are calculated from the complex-valued impedances. For the xy element, $\rho_{a,xy}$ is defined as

$$\rho_{a,xy}(\omega) = \frac{1}{\mu_0 \omega} |Z_{xy}|^2,$$

and the corresponding phase ϕ_{xy}.

$$\phi_{xy} = \tan^{-1}\left(\frac{\mathrm{Im}\,(Z_{xy})}{\mathrm{Re}\,(Z_{xy})}\right),$$

where $\omega = 2\pi f$ is the angular frequency and $\mu_0 = 4\pi \times 10^{-7}$ H/m the magnetic permeability of the vacuum.

While apparent resistivity is affected by galvanic distortion originating from localized near-surface heterogeneities, the phase response is free of such distortions, and provides a convenient way of visualizing the magnetotelluric response (Caldwell et al., 2004). The phase tensor is calculated from the complex impedance **Z** as

$$\mathbf{\Phi} = \mathrm{Re}\,(\mathbf{Z})^{-1}\mathrm{Im}\,(\mathbf{Z}). \tag{2}$$

Finally, the vertical transfer function **T**, commonly referred to as "tipper," is calculated as:

$$H_z = \begin{pmatrix} T_x & T_y \end{pmatrix} \begin{pmatrix} H_x \\ H_y \end{pmatrix} \tag{3}$$

We used the multivariate FFMT processing (Hering, 2019) as well as the ProcMT (provided by Metronix) processing tools to analyze the measured time series. For the FFMT processing, we used pairs of simultaneously recorded survey MT sites to implement a remote reference method. The distance between the local and reference sites ranges between 15 and 40 km. Single site ProcMT processing was used for periods <100 s for which the number of time segments did not allow robust statistical analysis. Consistency between apparent resistivity and phase was checked using the $\rho+$ criterion (Parker & Booker, 1996). Processing results at all sites with a $\rho+$ criterion shown by a solid line are presented in Supporting Information S1 (pp 7–38). The data quality was in general good, so that less than 5% of the raw data were removed using this criterion.

The data show a general trend of resistivity decrease with depth, as illustrated in Figure S1 in Supporting Information S1, superposing apparent resistivity and phases at all sites on one single plot. Figure 3 presents examples of transfer functions for three different sites, where the points represent the apparent resistivity and phase of the four impedance elements (Z_{xy}, Z_{yx}, Z_{xx}, and Z_{yy}), along with the corresponding error bars, later used in the inversion. Most of the data exhibit high quality, certainly because Sabancaya volcano is located far from possible noise sources. Interestingly, some stations in the northern part of the volcano recorded periods of up to 3000 s, enabling the investigation of deeper zones beneath Sabancaya.

Figures 4 and 8 depict the phase tensor (Booker, 2014; Caldwell et al., 2004) for the observed and predicted data, respectively. The phase tensor can be represented graphically as an ellipse, whose elongation is oriented in the direction of strongest resistivity gradient. They are shown here as ellipses alongside the induction vectors (Parkinson, 1962). This visualization offers a general view of the primary geoelectric characteristics present in the MT sounding prior to the inversion process. The ellipses are colored by the ϕ_2 phases defined as $\phi_2 = \sqrt{\det(\mathbf{\Phi})}$, presenting the geometrical mean of the principal phases (Booker, 2014). ϕ_2 values below 45° (cool colors) suggest an increase in resistivity with depth, indicative of more resistive media, while ϕ_2 exceeding 45° (warm colors) point to an increase in conductivity with depth. In the maps, at short periods (0.05 s; Figure 4a), high values to the east of the study area could indicate the presence of shallow conductors (in volcanic environments it is typically associated with the hydrothermal system). At a period of 20 s (Figure 4b), extremely high ϕ_2 phases are observed in the Huambo-Cabanaconde fault area. At lower periods Figures (100–200 s; 4c and 4d), high phases are detected at sites in the center of the survey, while at longer periods (500–1000 s; Figures 4e and 4f), phase values decrease at all sites to values near 45°, indicating an increase in resistivity at greater depths. These results suggest that the sounding data are sensitive to structures below the deepest conductive feature.

Induction vectors, as shown in Figures 4b, 4c, 8b, and 8c, are a graphical representation of the vertical transfer function **T**, and provide insights into the lateral heterogeneity of the subsurface (Parkinson, 1962; Wiese, 1962). Large vectors indicate abrupt conductivity changes, suggesting the presence of nearby conductive structures, such as the Huambo-Cabanaconde fault system, which runs parallel to the Colca Canyon. In contrast, small vectors reflect a more homogeneous medium with less pronounced resistivity gradients, as observed in Figures 4a and 8a. Finally, geoelectric strikes calculated using impedance and phase tensors are consistent with main geological lineaments in Figures S2 and S3 in Supporting Information S1. The strike directions are calculated with mtpy-v2 code (Kirkby et al., 2019) for the full frequency range of data, indicating heterogeneous resistivity at depth.

3.2. Magnetotelluric Inversion

The rough topography and heterogeneity in the area of interest requires 3D modeling. We employed the frequently used inversion code ModEM (Kelbert et al., 2014), based on a structured-grid finite integration forward model, implementing a Bayesian approach (Rodgers, 2000; Tarantola, 2005). Defining the objective function

$$\begin{aligned} \Theta &= (\mathbf{g}[\mathbf{m}] - \mathbf{d})^T \mathbf{C}_d^{-1} (\mathbf{g}[\mathbf{m}] - \mathbf{d}) + \\ &\qquad \lambda (\mathbf{m} - \mathbf{m}_a)^T \mathbf{C}_m^{-1} (\mathbf{m} - \mathbf{m}_a) \\ &= \|\mathbf{C}_d^{-1/2} (\mathbf{g}[\mathbf{m}] - \mathbf{d})\|^2 + \lambda \|\mathbf{C}_m^{-1/2} (\mathbf{m} - \mathbf{m}_a)\|^2, \end{aligned} \tag{4}$$

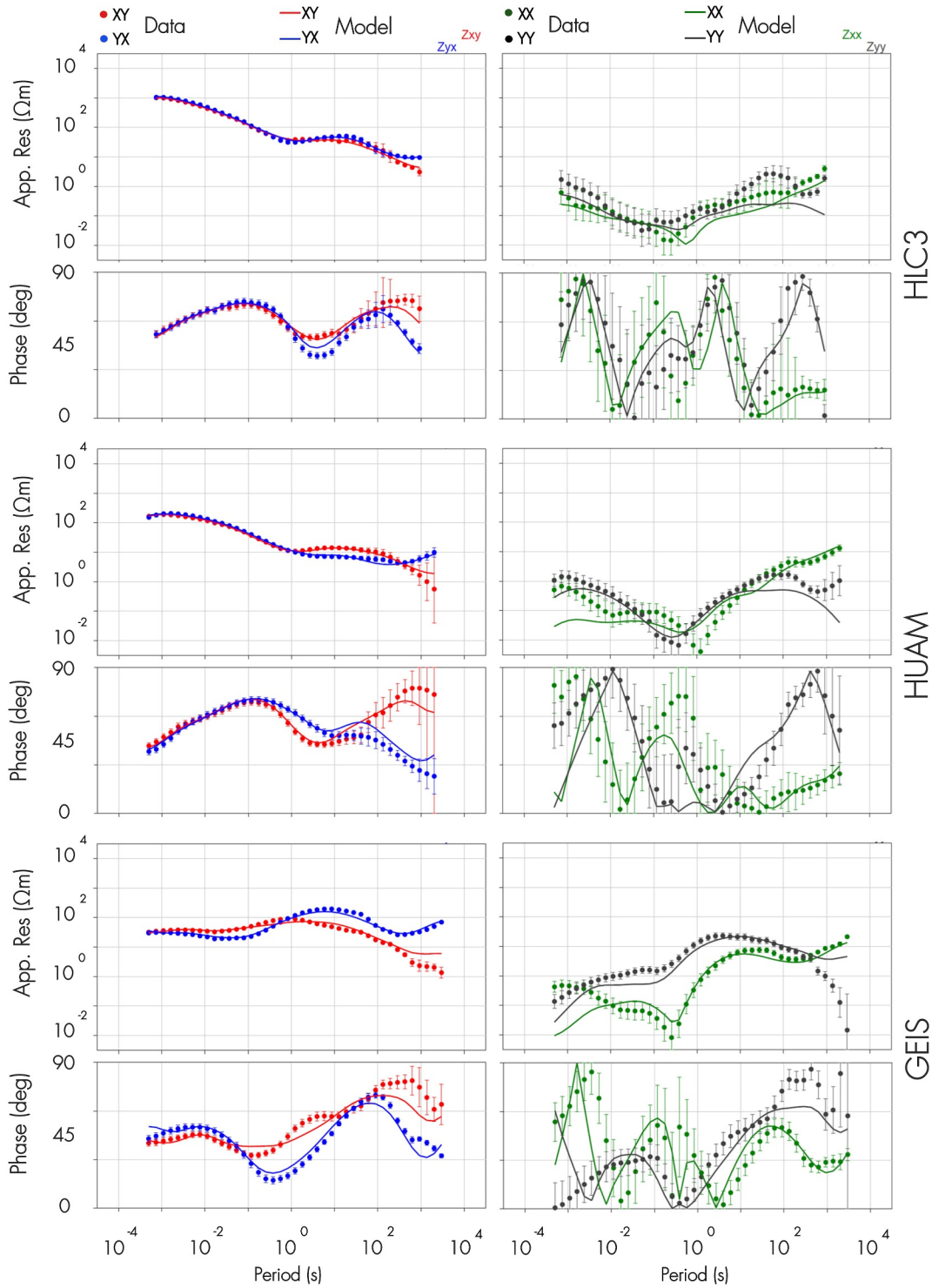

Figure 3. Examples of apparent resistivity and phase curves of the impedance tensor for sites HLC3, HUAM, and GEIS. The apparent resistivity (upper panels) and phase (lower panels) calculated from the off-diagonal and diagonal elements of **Z** are shown as an example of data quality. Dots represent the observed data while the plain lines represent the predicted data obtained from the best 3D electrical model obtained after inversion, and discussed in Section 4.

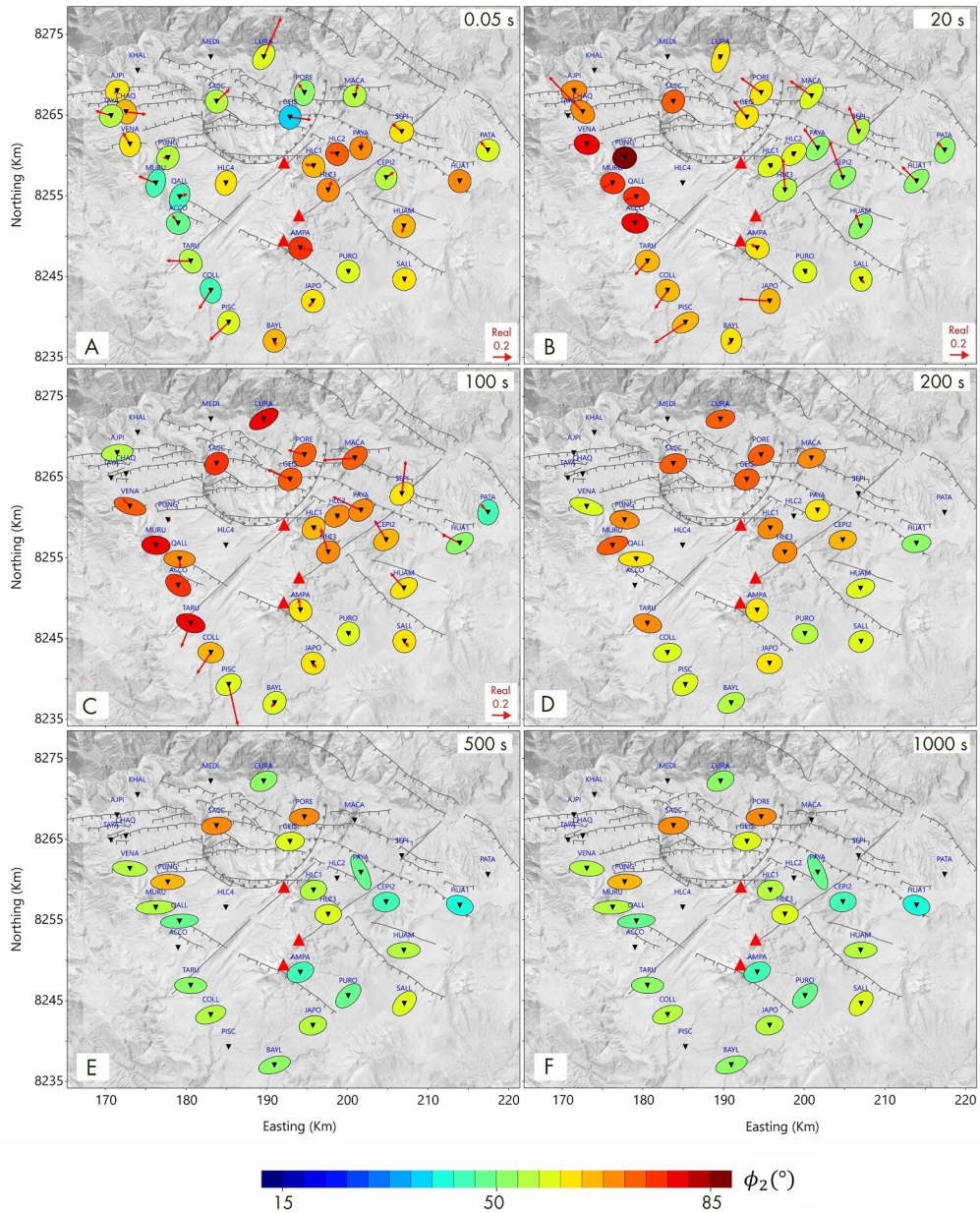

Figure 4. Phase tensor obtained from measured data represented as ellipses for different periods (in seconds). Color scale quantifies ϕ_2, the geometric average of the principal phases. Red arrows represent the induction vectors (see Figures a–c). High phases, highlighted by warm colors, correspond to decreasing resistivity with increasing depth, while cool colors indicate increasing resistivity with depth.

the final model is obtained iteratively, minimizing the objective function defined in Equation 4. This equation combines two terms, where the first describes the misfit (the difference between the observed and predicted data) and the second is a regularization term. Here, **d** is the data vector, **m** is the model vector, λ is a trade-off parameter, and $\mathbf{C}_d^{-1}$ and $\mathbf{C}_m^{-1}$ are the inverse prior data and model covariances.

The former is assumed diagonal, containing the observational errors, i. e., the squared standard deviation σ_i^2 in a Gaussian framework. The implementation of the latter in ModEM is based on an exponential covariance, which means that the spatial part is proportional to the term $\exp\left(-\frac{|\mathbf{r}_{ij}|}{L}\right)$ in each direction, where $\mathbf{r}_{ij}$ is the distance between points i and j in the model, and L is a correlation length, determining the area of influence. Note that in

Table 2
Magnetotelluric Acquisition and Modeling Parameters

Acquisition		
Acquisition duration (h)		20–40
Data used (s)		10^{-3} to 3000
Processing		FFMT, ProcMT
Model parameters		
Mesh	Horizontal	67 × 79 cells (950 m × 950 m)
		13 padding cells
	Vertical	105 cells
		Initial 90 m, Increase factor 1.1
Error floors	Impedance	
		$\sigma_{Zxx} = 0.1\sqrt{\lvert Z_{xx}Z_{xy}\rvert}$
		$\sigma_{Zyy} = 0.1\sqrt{\lvert Z_{yx}Z_{yy}\rvert}$
		$\sigma_{Zxy} = 0.05\sqrt{\lvert Z_{xy}Z_{yx}\rvert}$
		$\sigma_{Zyx} = 0.05\sqrt{\lvert Z_{xy}Z_{yx}\rvert}$
Fixed error	Phase tensor	
		$\sigma_{Pxx} = \sigma_{Pyy} = 0.15$
		$\sigma_{Pxy} = \sigma_{Pyx} = 0.2$
Fixed error	Tipper	
		$\sigma_{Tx} = 0.03$
		$\sigma_{Ty} = 0.05$
Parameter α		0.3, 0.1
Final nRMS		1.36

ModEM, the $r_{i,j}$ and L values are measured as the difference of cell indices, not physical distance. The prior parameter covariance matrix $\mathbf{C}_m$ and its inverse are never formed explicitly, but the action of the corresponding square root on the parameter vector $\mathbf{m}$ is realized through successive autoregressive one dimensional filters, controlled by parameters $\alpha_{i,j,k}$ for the corresponding directions. Their values are required to be between 0 and 1, and related to the desired correlation length defined as $L = -\frac{1}{\ln \alpha}$. We inverted impedances, tippers, and phase tensors, gradually decreasing α, thus allowing more roughness in the model. In the framework of ModEM, this amounts to reducing the spatial correlation length for the prior parameter covariance.

To achieve an optimal balance between the regularizing second term in Equation 4 and the data fit, a trade-off parameter, λ, is introduced. In the framework of ModEM, λ is determined internally, starting from a value given by the user, and successively decreasing until no further improvement of the fit occurs. Details can be found in Egbert and Kelbert (2012) and Kelbert et al. (2014).

A mesh with a horizontal cell dimension of 950 m × 950 m in the core area with 41 × 53 cells was set up. Outside the core, the cell sizes increased by a factor of 1.3 in both directions, in order to satisfy the respective boundary conditions. In this way, the core area of about 38×50 cells is embedded in an approximately 280 km × 290 km horizontal mesh. Vertically, 105 cells were used, with sizes starting from a thickness of 90 m increasing by a factor of 1.1 downwards, representative of the diffusive nature of the electromagnetic signals used in MT. This mesh size and increase factor was chosen to balance computational efficiency and model resolution. High resolution topographic data were used (https://www.gmrt.org), subsequently interpolated from the original 30 m to fit the horizontal mesh of the model.

To prepare the data for the inversion, errors for the observations need to be provided. There are several effects which may produce very small errors in the impedances. One is a purely statistical effect, as a consequence of the very high numbers of spectra at high frequencies produced by frequency domain processing. However, reliable estimates in MT require the satisfaction of a few more assumptions. One problem can originate from the dominating highly polarized signals, usually but not always produced by man-made sources. These will also display high coherencies, and thus small errors. For the former, the common remedy of introducing error floors to reduce their influence is useful. Unfortunately this is not possible in the case of bias due to source field characteristics (e.g., near-field effects in man-made noise, or the Equatorial Electrojet (EEJ)), which need to be treated otherwise. In the case of the data under consideration a contamination by man-made coherent noise is neither probable nor evident. We will return to a possible bias by the non-uniform and time-dependent electrojet below.

MT works with time series which contain information on a frequency range of more than 6 decades. As the absolute values of the impedances can vary over several orders of magnitude, the error floors for the impedance components were defined as relative errors, with the off-diagonals on their geometric means and the diagonals on geometric means of the rows of the impedance tensor. Fixed errors were assigned to phase tensor and tipper components. Please refer to Table 2 for settings, and error definition on all inversion parameters: impedance (Z), phase tensor (P), and tippers (T).

Figure 5 shows the workflow of the 3D inversion, which was carried out in three stages to improve the resolution of the resistivity model, at the same time ensuring numerical stability. First, a joint inversion of impedance and tipper (ZT) was performed, using various prior models with the default parameter $\alpha = 0.3$, chosen after performing trial and error tests (not shown here). A prior homogeneous model of 20 Ωm provided the best fit to the observed data (see Figure S1 in Supporting Information S1). In the second step, the resulting model was used as prior model for the inversion of the phase tensor (P) with $\alpha = 0.3$. Basing on the results of this step, a static shift correction was applied, and a new impedance inversion (Z) was performed with a smaller smoothing ($\alpha = 0.1$).

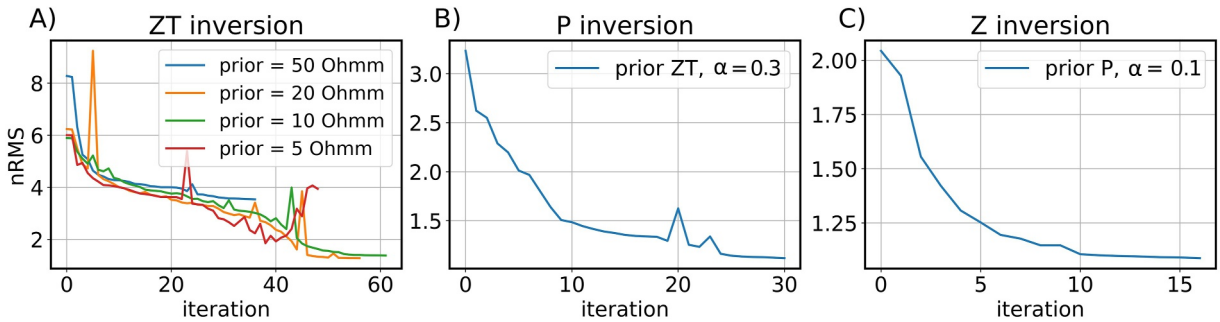

Figure 5. Steps followed for the 3D inversion of the Ampato-Sabancaya complex and Hualca-Hualca volcano MT data. (a) The impedance and tipper data were inverted with different prior models, with the best fit obtained for 20 Ωm. (b) Using the best impedance inversion model as a prior model $\mathbf{m}_a$, the phase tensor was inverted. Using the best phase tensor (P) inversion, we applied a static shift correction to the data. (c) The shift-corrected impedance tensor was inverted again with a smaller α, allowing more structure.

This strategy enabled capturing increasing structural complexity in the subsurface. As a result of this sequential inversion, a final *nRMS* of 1.36 was obtained. The *nRMS* is a common measure of the data fit, defined by

$$nRMS = N_d^{-1/2} \|\mathbf{C}_d^{-1/2}(\mathbf{g}[\mathbf{m}] - \mathbf{d})\|, \quad (5)$$

where $\mathbf{d}$ is the vector of observed data, $\mathbf{g}[\mathbf{m}]$ is the corresponding model prediction, and N_d is the number of observations.

As the magnetic equator crossed Peru, one may suspect that the Equatorial Electrojet (EEJ) and related phenomena may influence the observations and thus our models. Sabancaya is more than 600 km (6°) away from the magnetic dip equator, which is currently slightly north of Lima (https://www.ncei.noaa.gov/products/world-magnetic-model). While we can not rule out an influence of the EEJ on our data, we think it is minor and only influences our modeling weakly from the results discussed below.

It is well known that the largest influence occurs in $\mathbf{H}_z$ entering our modeling only through the tippers in the first step. It is detectable mainly at long periods >100 s, where scatter and error bars are already larger due to the smaller number of samples. Due to issues beyond our control, we could only use tipper measurements at 12 sites, and not at all periods.

The impedance is believed to be less affected than the tipper. The classical studies on EEJ interference with MT (Dmitriev & Berdichevsky, 1979; Padilha, 1999; Padilha et al., 1997; Viljanen, 2012) all agree that the effect on MT impedances is not significant in the period range considered here. Dmitriev and Berdichevsky (1979) argued that, above a layered Earth, MT data can be interpreted in the usual way even when the source field varies linearly over a scale of up to three skin depths. Analyzing MT results in a 5° strip around the magnetic equator (Padilha, 1999; Padilha et al., 1997) conclude that even for the worst case of high subsurface resistivity, the MT impedances change little up to periods of 1000 s. Around Sabancaya the average subsurface resistivity is quite low (≈10 Ωm).

4. Results

Examples of the transfer function differences between observed data and predicted data at three sites are shown in Figure 3. The off-diagonal elements of the impedance are predicted better than the main-diagonal, but in general the misfit is relatively low. The quality of the data fit can also be evaluated comparing the observed phase tensors (Figure 4) with predicted phase (Figure 8).

Figures 6, 7, and 9 show horizontal and vertical sections extracted from the final 3D resistivity model. They are characterized by strong lateral resistivity contrasts at shallow and intermediate depths, and generally low resistivity below. In the following, we focus on the main conductive features labeled C1 to C3 (Table 3).

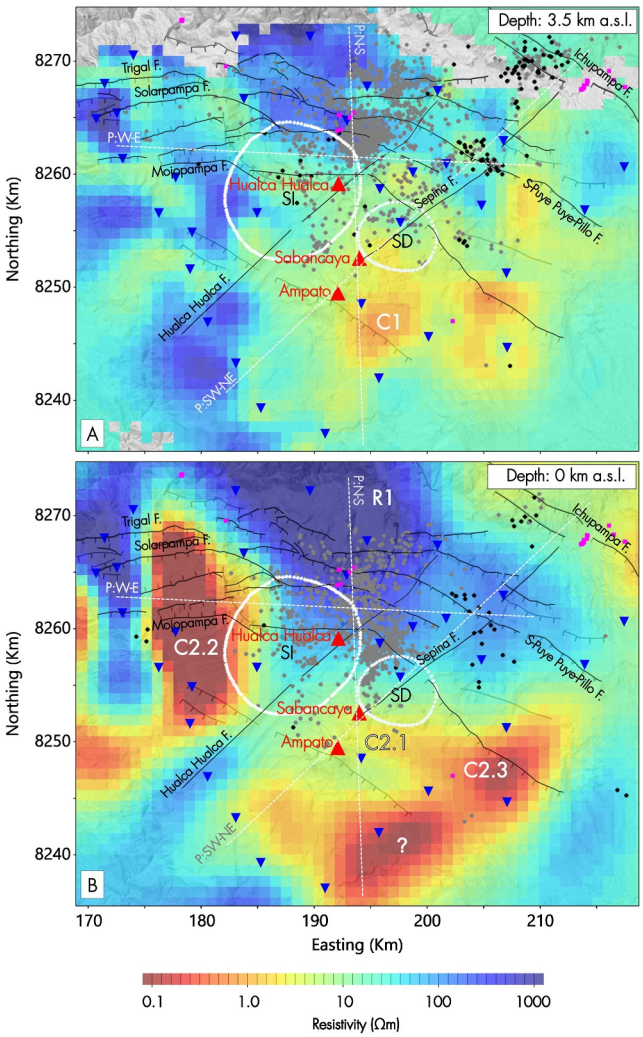

Figure 6. Horizontal sections extracted from the 3D resistivity model, combined with corresponding seismicity. Black dots mark pre-eruptive stage earthquakes (2013–11/2016), gray dots are from the co-eruptive stage (11/2016–2020). The locations of the N-S, W-E and SW-NE vertical sections in Figures 9 and 10 are shown in white dashed lines. (a) Horizontal slice at 3.5 km a.s.l. (seismic events from depth interval 4.2–2.5 km a.s.l.). (b) Horizontal section at 0 km a.s.l. (seismic events from depth interval 2.5–1 km b.s.l.).

4.1. Surface Conductor C1

The C1 conductor has a resistivity ranging between 1 and 10 Ωm, with the top of this body located between 5.0 and 3.5 km above sea level beneath the Sabancaya-Ampato and Hualca-Hualca volcanoes, where it is overlain by a high resistivity layer (≈100–1,000 Ωm). Its geoelectric properties are variable and show patterns that follow the volcanic topography, and it extends in a southeast-northeast direction from Sabancaya toward the Sallalli and Sepina areas (Figures 6, 7, and 9).

Superimposing C1 with seismicity between 4.2 and 2.5 km a.s.l. shows that most of the earthquakes occurred during the co-eruptive phase, clustered north of Hualca-Hualca volcano, while only a few earthquakes were recorded during the pre-eruptive phase, mainly located along the distal faults (Figure 6a). Seismic grouping is observed outside and 10 km northeast of the maximum deformation, within the resistive zone. At this depth level, the earthquakes do form seismic groups in the Maca area. In addition, two other groups occurred during the pre-eruptive and eruptive stages: the closest is distributed 12 km from Hualca-Hualca, where a reverse fault that intersects the Sepina fault; the second group is located 20 km from the Hualca-Hualca, where the Ichupampa normal fault was reported as reactivated in August 2016 (Machacca et al., 2023; Tavera et al., 2016), and presents a distribution aligned with the northeastern end of the Sepina fault.

4.2. Intermediate Conductors C2

To the northwest and southeast of the surface inflation zone, three conductors (C2.1, C2.2, and C2.3) are observed. The conductor C2.1 varies in depth from approximately 3 km a.s.l. to 2 km b.s.l., beneath Sabancaya, slightly offset to the east of the volcano. It has a relatively homogeneous resistivity between 1 and 5 Ωm. Vertical cross-sections (Figure 9a) show that, C2.1 is directly connected to conductor C3. On the vicinity of C2.1, a 6 cm deflation zone was recorded by InSAR imagery in 2013 (Jay et al., 2015; Torres, 2014). Overlain with seismicity in the depth interval from 2.5 km a.s.l. to 1 km b.s.l., it indicates that C2.1 lies within an aseismic zone. A petrological study by Gerbe and Thouret (2004) associates this aseismic sector with a shallow magmatic chamber of Sabancaya located at approximately 6 km depth, which is consistent with our model of this low-resistivity zone.

At intermediate depths, the C2.2 conductor has an extremely low resistivity, lower than 0.1 Ωm. It is located northwest of the Sabancaya volcano and of the western sector of maximum deformation, between approximately 3 km a.s.l. and 7 km b.s.l. beneath the Huambo-Cabanaconde fault system. It then extends southeastward to a depth of down to 14 km b.s.l. However, the southeast sector of the C2.2 anomaly has a poor MT sounding coverage, and its extension may reflect an inversion artifact. Also, C2.2 lies over a highly resistive zone (R2) of up to 1000 Ωm. Compared to the seismicity in the depth interval from 1 to 6 km b.s.l, the northwest sector of C2.2 is seismically quiet. As it deepens, it connects with anomaly C3, in a transition zone marked by a seismic grouping only observed during the pre-eruptive stage of the Sabancaya volcano. This seismic sequence and observed surface deformation from July 2013, are associated with the activation of the Solarpampa and Triga normal faults (Jay et al., 2015; Machacca et al., 2023; Tavera et al., 2013).

C2.3, to the South and East beneath Ampato volcano, lies between approximately 2 km a.s.l. and 6 km b.s.l., with a northeast to southeast direction, extending over 25 km. Resistivities lower than 1.0 Ωm are observed.

At a depth of 5 km b.s.l., an overlap between conductors C2.3 and C3 is observed in a region coinciding with a seismic grouping which was monitored during the pre-eruptive and eruptive stages.

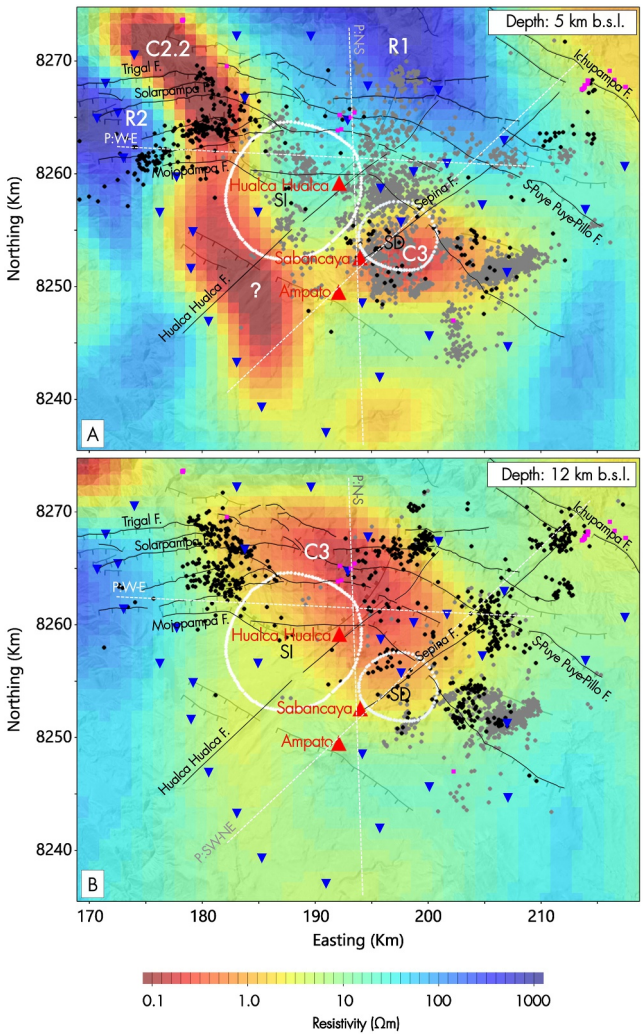

Figure 7. Horizontal sections extracted from the 3D resistivity model, combined with corresponding seismicity. Black dots mark pre-eruptive stage earthquakes (2013–11/2016), gray dots are from the co-eruptive stage (11/2016–2020). (a) Horizontal slice at 5 km b.s.l. (seismic events from depth interval 1–6 km b.s.l.). (b) Horizontal slice at 12 km b.s.l. (seismic events deeper than 6 km b.s.l.).

Figure 6b shows a highly resistive feature located between the C2.2 and C2.3 bodies coinciding with a fault, which we call here the Hualca-Hualca fault, with a northeast-southwest orientation. At the northeastern end of the fault, at depths between 2.0 km a.s.l and 1 km b.s.l., a seismic group recorded during the co-eruptive phase can be observed.

4.3. Deep Conductor C3

The C3 conductor is located northeast of the maximum deformation and north-northwest of the Sabancaya volcano. It has a size of 25 km in length and 15 km in width. The top of the conductor is located between approximately 5 and 6.5 km b.s.l. and continues down to approximately 12 km b.s.l. beneath the Hualca-Hualca volcano. Conductor C3 has resistivity ranging between 0.2 and 0.5 Ωm. Above C3 there is a highly resistive zone of up to 1000 Ωm (R1).

The seismicity in the depth interval from 6 to 17 km b.s.l. indicates clusters of earthquakes along the border of the C3 conductor, with a low seismicity zone located inside the anomaly (C3, Figure 7d). At this depth level, the earthquakes were mostly recorded in the pre-eruptive stage and are observed along normal and reverse faults.

4.4. Sensitivity Study

In order to understand whether our observations constrain certain prominent conductive features of our model, we applied nonlinear tests similar to the ones proposed in Nolasco et al. (1998); Heise et al. (2024). To establish that our model requires resistivity values less than 1 Ωm, we replaced conductive anomalies below 1 Ωm (such as anomalies C2.2 and C3) with a homogeneous value of 1 Ωm and subsequently performed forward modeling to compare the synthetic and observed data. The results indicate that the nRMS dramatically increases, especially at frequencies below 0.1 Hz (10 s), and at stations CHAQ, MURU, GEIS, and HLC3 (see Figure 11).

Figure 12 compares the nRMS of observed data and synthetic data generated for a model perturbed in the described manner for different resistivity thresholds. Similar as in previous Figure, the model resistivities lower than a threshold value in a set (0.001, 0.01. 0.1, 0.2, 0.4 Ωm) were replaced with this threshold value and synthetic data were created and compared to the observations. The data were considered in different frequency ranges and Figure 12 shows a significant nRMS increase, especially at low frequencies. Note that the number of perturbed cells depends on the threshold and decreases with the decrease of the threshold value. In an extreme case of $\rho_{thres} = 0.001$ Ωm, there are no model cells below this threshold and there is no model perturbation; the nRMS value will in this case will be the nRMS of the best model. This sensitivity study suggests that the presence of highly conductive anomalies are well constrained by the data, including low frequencies/greater depths.

Sensitivity studies concerning C2.1 and C3 bodies are presented in the Supporting Information S1 (Figure S4). They include nRMS-vs-resistivity plots to define the uncertainty of the model resistivity of these bodies. As follows from Figure S4c in Supporting Information S1, resistivity of the C2.1 body has an optimal value of 1–5 Ωm. Figure S4f in Supporting Information S1 shows nRMS against resistivity plot for C3 body, with resistivity close to 0.4–0.6 Ωm (see section "Sensitivity study for C2.1 and C3 bodies" of Supporting Information S1).

5. Discussion

5.1. Seismicity Distribution as Indication of Aseismic Behavior

Seismicity is intimately related to the matrix rheology (Amitrano, 2003) and can be used to reduce the parameter space of possible melt fraction estimations. We consider the distribution of seismic events as a function of

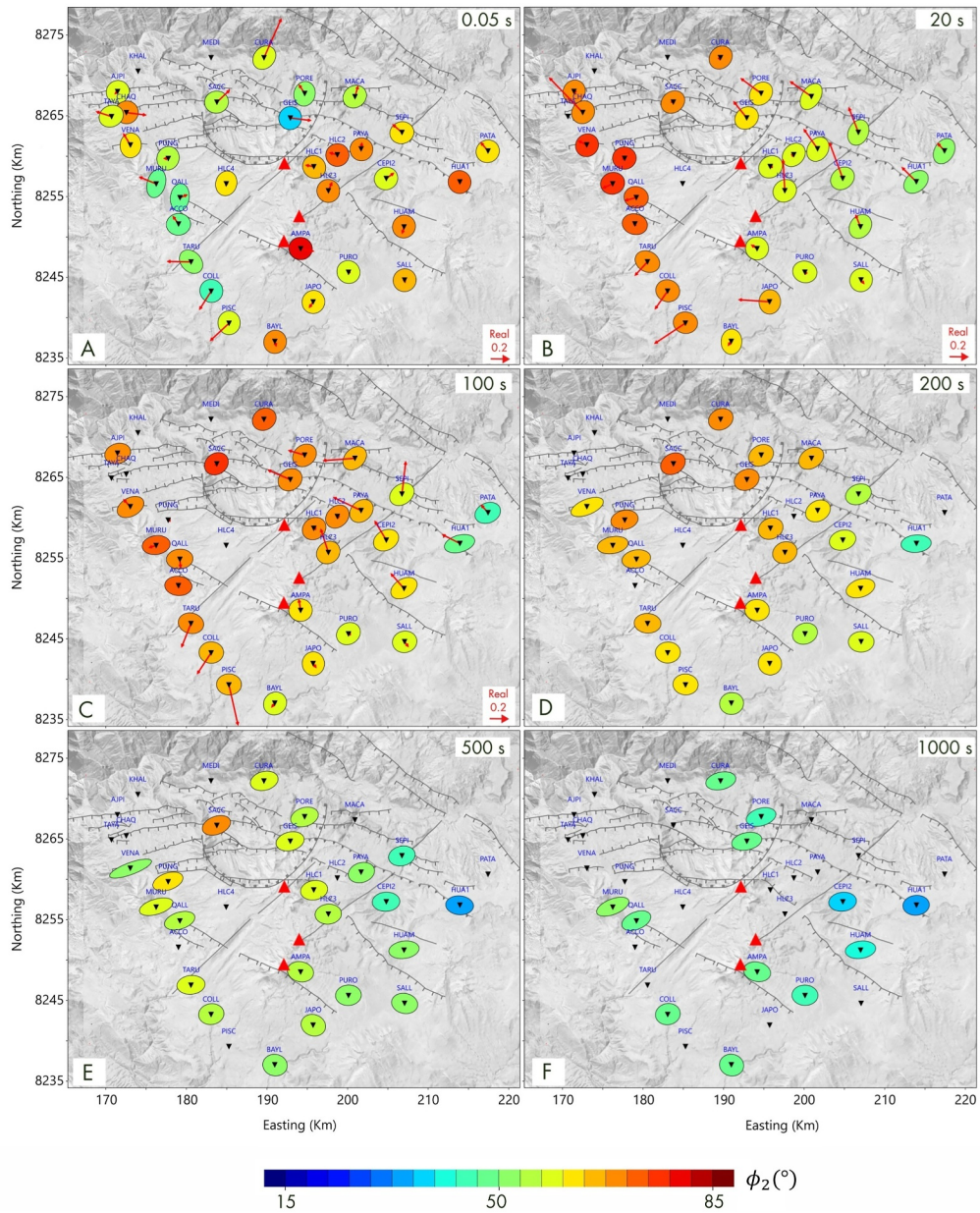

Figure 8. Phase tensors predicted by the best model obtained after inversion for the same frequencies as shown in Figure 4. Similarity with the Figure 4 demonstrates the quality of the inversion process that captures the principal features of the data.

electrical resistivity to find a minimum value of model cell resistivity for which seismic events can still occur (resistivity of aseismic transition).

To this end, we calculate the number of seismic events and the corresponding moments for the model cells located in the central part of our model, namely, inside an ellipsoid with x, y, and z semi-axes 23, 28 and 14 km, centered at a depth of 6 km b.s.l. with geographical coordinates [−15.767, −71.854]. Air and padding cells are excluded. The resulting seismicity-resistivity plot is shown in Figure 13.

For simplicity, we consider first the depths below 4 km b.s.l. only (8 km below the surface), taking into account the bimodal distribution of seismicity (Figure 13c). Splitting the distribution according to depth provides a simple possibility to separate the mush and deep magma reservoir (C3 conductor) from the shallow magma chamber C2.1, hydrothermal fluids and their alteration products (C1), or exsolved magmatic brines (C2.2). At a greater depth, we assume the conductors to represent magmatic bodies with high enough melt content.

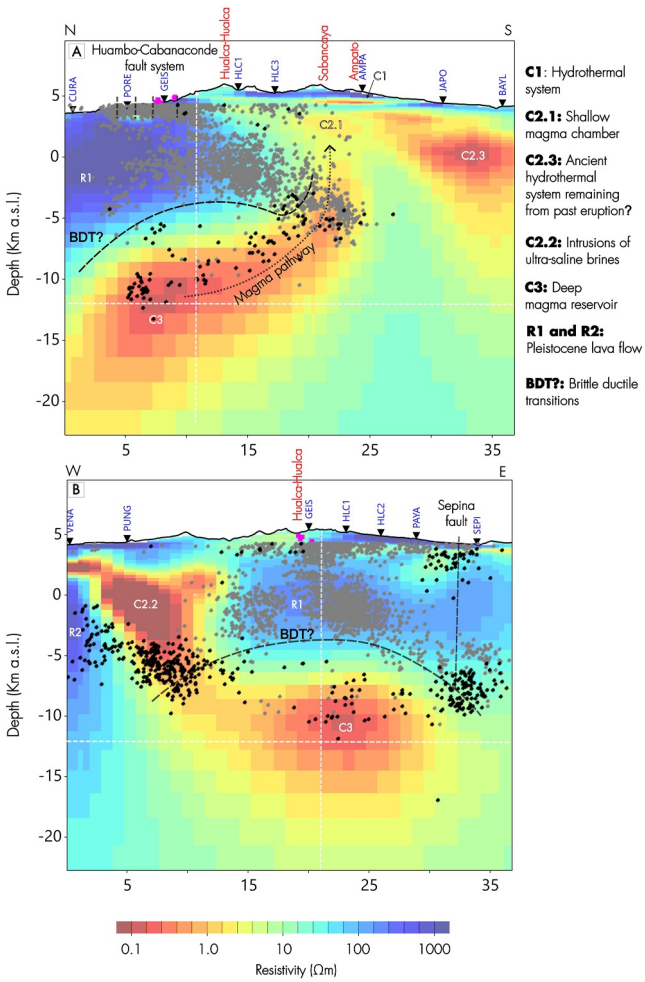

Figure 9. Vertical sections extracted from the 3D resistivity model. Each section shows seismic events within a 4.0 km section, where black dots represent pre-eruptive stage earthquakes (2013–11/2016), gray dots refer to the co-eruptive stage (11/2016–2020). The black dashed line shows tentatively ductile-brittle transition zone (BDT) qualitatively based on seismic distribution and MT model. Vertical black dashed lines represent known distal faults. White dashed lines show the intersection of the N-S and W-E vertical sections and a horizontal section at 12 km b.s.l (Figure 7 B). Magenta symbols represent hydrothermal manifestations. (a) N-S section through the Hualca-Hualca, Sabancaya, and Ampato volcanoes. (b) W-E section through the Hualca-Hualca volcano.

We define the resistivity of aseismic transition as a break point of the seismic moment-resistivity distribution, marked by a dashed red line in Figure 13b. The threshold corresponds to a 8%–10% percentile, or a resistivity value of $\rho_{aseismic}$ ≈0.6 Ωm. Almost 15% of deep seismic events occur at low resistivities, <1 Ωm (for comparison, the resistivity of the seawater is 0.3 Ωm). Such low resistivity values obtained at more than 8 km below the surface are indicative of magma reservoir with relatively high partial melt and/or water content, which will be discussed below.

5.2. Some Speculations About the Evolution of Electrical Resistivity Structure

Figures 13c–13f shows similar scatter plots including a full depth range, considering both co-and pre-eruptive catalogs. Noteworthy, the pre-eruptive seismicity is plotted against the co-eruptive resistivity structure (Figures 13e and 13f). The shift toward lower resistivities values between Figures 13c–13f may be attributed to the alteration of rocks that have occurred since the onset of the current eruptive process. It is important to keep in mind that only a 2022 snapshot of electrical resistivity is available, while the seismicity was recorded over several years of changing volcanic activity. Following MacQueen et al. (2020), the pre-eruptive activity, with the strongest events reaching the magnitude Mw = 5.9, has created pathways for magmatic fluids, which could have lead to a significant change of the electrical and mechanical properties of rocks. In a pre-eruptive period of 2013–2016, close to 90% of seismic events occurred and up to 90% of seismic energy were released in an environment that in 2022 is characterized by resistivity below 10 Ωm. In the following, we consider the evolution of the resistivity structure since the onset of eruptive process negligible in comparison with strong horizontal and vertical contrasts of the resistivity model. In other words, we consider co-eruptive seismicity as contemporary with the resistivity model.

5.3. Melt Fraction and Porosity Estimates

Four main conductive features (C1, C2.1, C2.2, C2.3, and C3) are identified from the best resistivity model (Figures 6–10), their parameters are summarized in Table 3. The deep C3 body is tentatively identified with the magma reservoir, while the shallow C1 could be the signature of aqueous fluids as suggested by Self-Potential (SP) studies (Alvarez, 2017; Puma et al., 2018). Interpretation of the intermediate depth features is less straightforward as both magmatic and aqueous fluids can be present at intermediate depths.

The presence of crustal fluids (aqueous or magma) reduces the mechanical strength of rocks, and generally decreases the electrical resistivity (Aizawa, 2016; Becken et al., 2011; Liu & Hasterok, 2016). The transition from a solid-state to a melt-dominated creep rheology has been extensively

Table 3
Summary of the Analysis of the Five Conductive Anomalies

Feature type	Name	ρ_{avg} Ωm	Depth (km above sea level)	Depth (km below surface)
Magma bodies	C2.1	1.0–5.0	3.0–−2.0	3.0–8.0
	C3	0.2–0.5	−5.0–−12.0	11.0–18.0
Magmatic fluids	C2.2	0.1	3.0–−5.0	2.0–10.0
	C2.3	0.1	2.0–−6.0	2.0–10.0
Hydrothermal system	C1	1.0–10.0	5.0–3.5	1.0–2.0

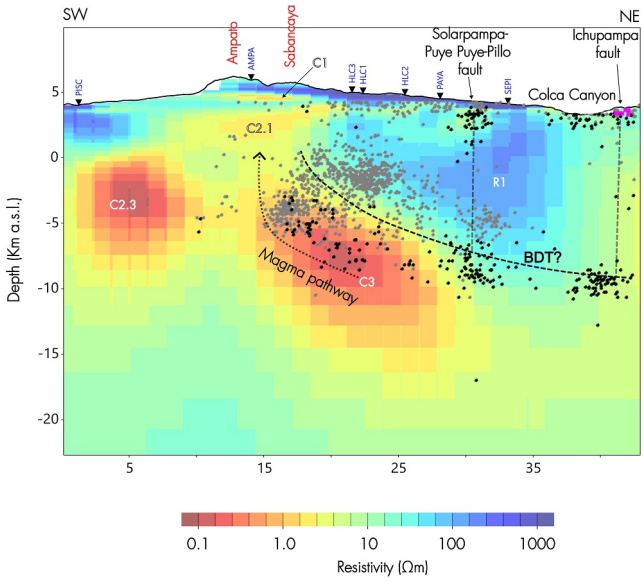

Figure 10. Vertical section parallel to the Sepina fault. The black and gray points represent pre- and co-eruptive seismicity. The vertical dashed lines represent distal faults discussed in Section 5.5.

studied (Arzi, 1978; Nur et al., 1998; Takeda & Obata, 2003; Vigneresse et al., 1996). To quantify this transition, threshold values of melt fraction were introduced: (a) a liquid percolation threshold above which melt pockets can connect (≈0.08), ductile deformation occurs, while seismic shear velocity decreases; (b) a critical melt fraction near 0.3–0.4, above which the large scale deformation is possible and melt behaves as liquid and can be considered eruptible (Arzi, 1978; Bennington et al., 2025; Takeda & Obata, 2003; Vigneresse et al., 1996). The eruptible magma threshold can also be seen as a boundary between the ductile domain where the seismicity is still possible, and the domain where shear failure is not possible anymore. According to this reasoning, seismicity is an indicator of the magma melt fraction being below the critical porosity of 0.35 ± 0.05.

To link the distribution of electrical resistivity to the melt fraction (related to the rheology of the crust), we first need to know the resistivity of the melt. For andesitic magma, we use the empirical equation established by Laumonier et al. (2017) connecting the conductivity of the melt σ_f at a given temperature T, pressure P and water content w. Figure 14a shows calculated melt conductivity for an andesitic composition under temperature-pressure conditions and water saturation levels consistent with experimental petrology results (Gerbe & Thouret, 2004).

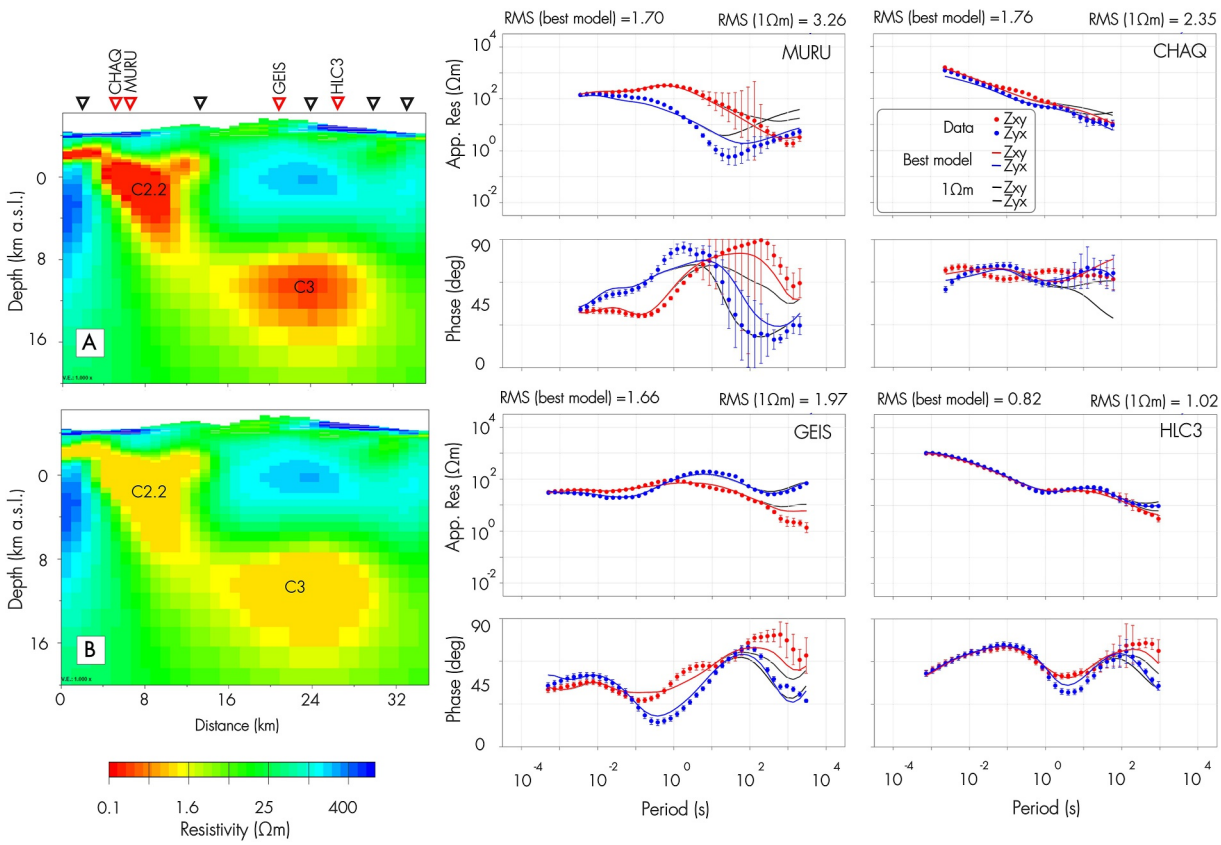

Figure 11. Sensitivity analysis performed for the main anomalies C2.2 and C3. The profiles on the left side show: (a) the best resistivity model, and (b) the edited resistivity model, where resistivities lower than 1 Ωm were replaced with this threshold value. The graphs on the right side compare the measured data with the response of the calculated data after editing the resistivity model for stations MURU, CHAQ, GEIS, and HLC3, respectively. Additionally, the nRMS of the best resistivity model and the nRMS of the edited resistivity model are displayed above the graphs.

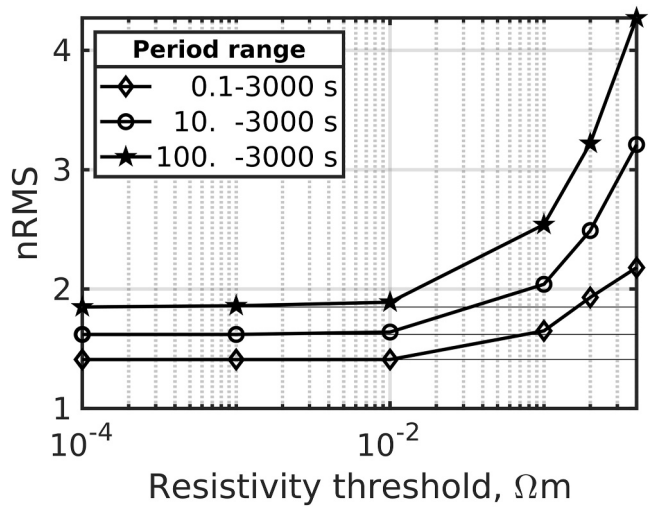

Figure 12. nRMS between the best and perturbed models (as shown in previous Figure) for various threshold values of resistivity. Note that the number of perturbed cells depends on the threshold and decreases with the decrease of the threshold value. At very low threshold values, the nRMS converges to the best model because very little or no perturbation are applied.

In a next step, the magma fraction can be estimated by comparing the theoretical melt resistivity and the bulk resistivity determined from 3D inversion of field data. To this end, we use the modified Archie's law, which relates bulk conductivity σ_b to melt fraction ϕ, conductivity of rocks σ_r, and pore fluids or melts σ_f as (Glover et al., 2000):

$$\sigma_b = \sigma_f.\phi^m + \sigma_r(1-\phi)^p, \quad (6)$$

where m is melt connectivity exponent, and p is calculated as:

$$p = \frac{\log(1-\phi^m)}{\log(1-\phi)}.$$

When $m = 1$, the fluid phase in the rock matrix is fully connected, whereas larger values of m indicate lower connectivity. Equation 6 was used to estimate the melt fraction of the volcanic magmatic bodies using our resistivity distribution (Bennington et al., 2025; Comeau et al., 2016; Cordell et al., 2022; Samrock et al., 2021). Figure 14 B illustrates this approach for the estimation of the melt fraction applied to the C2.1 body. Noteworthy, as discussed by Heise et al. (2024), this evaluation critically depends on the accuracy of the resistivity model. In our case, the sensitivity tests presented in Section 4.4 (Figure 11) indicate that the acquired data are sensitive to the depth where the deep magmatic reservoir is expected (conductor C3).

Finally, to reduce the parameter space, we used the fact that two parameters strongly influencing the observed resistivity, namely the temperature of the magma and its melt content are inter-related. Based on Mount Pelee data samples, Annen et al. (2008) established an empirical relationship between the temperature of andesitic magma and melt fraction that can be used to reduce the number of possible solutions (Figures 14c and 14d). This approach was used here for all features independently.

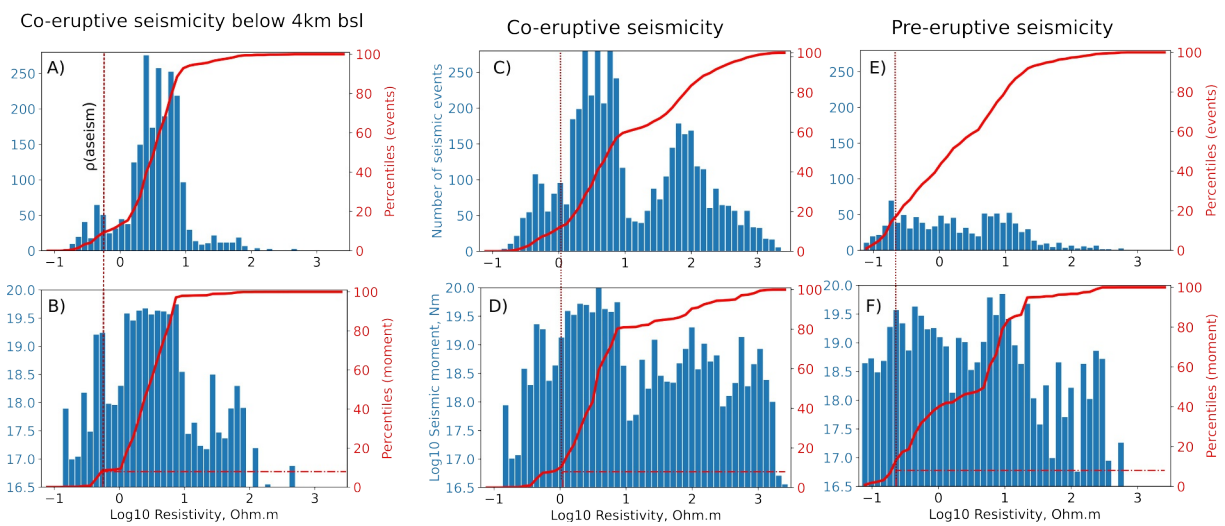

Figure 13. Seismicity-resistivity scatter plots calculated using the central cells of the resistivity model. (a, b) Co-eruptive seismicity-resistivity distribution below 4 km b.s.l. The broken red lines show two breaks of the cumulative energy curve (b) observed at 8%–10% of the total cumulative seismic moment. We take these values as proxy for the range of the aseismic magma rheology at greater depth. (c–f) Co- and pre-eruptive seismicity-resistivity distributions for the full depth range. Upper panels show number of seismic events while lower panels show seismic moment calculation.

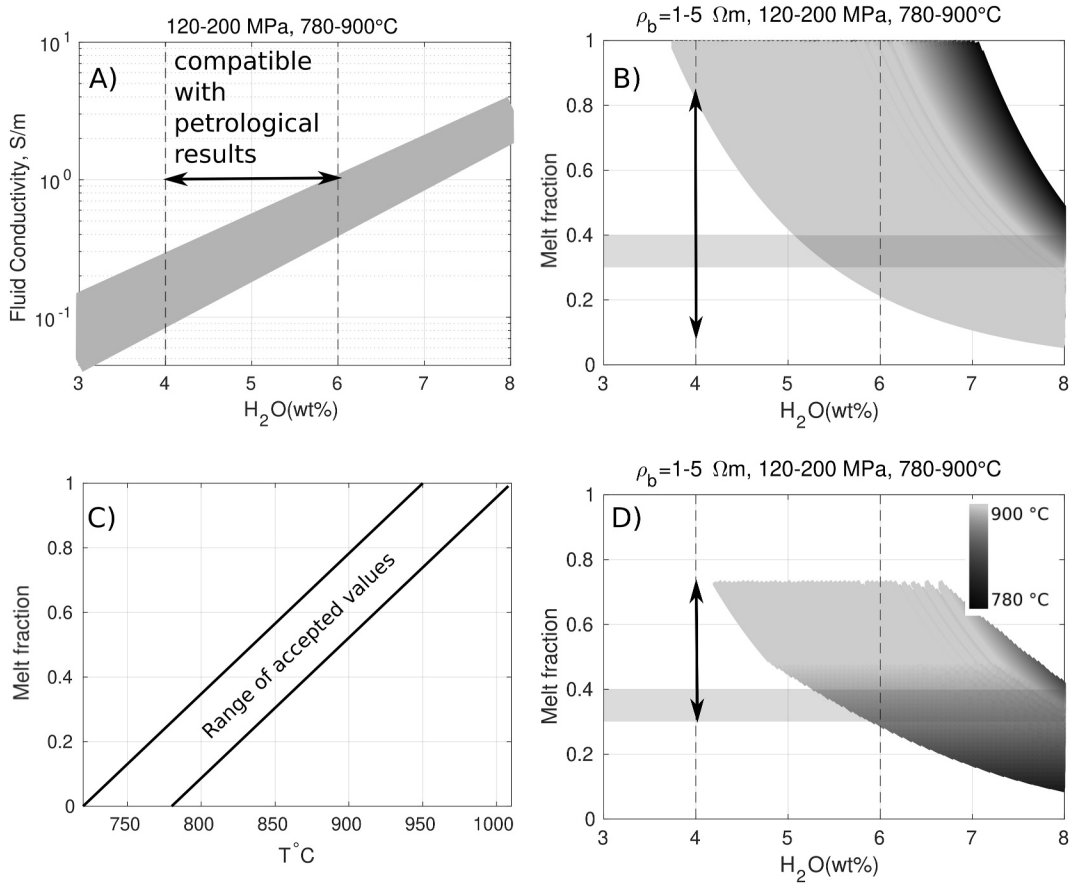

Figure 14. (a) Relationship between the conductivity of the melt σ_f at a temperature T, pressure P, and the water content w after (Laumonier et al., 2017), applied for C2.1 body. For comparison, horizontal arrow shows the range of the water content values 4–6 wt% expected from petrological observations (see text). (b) Andesitic magma fraction calculated from this theoretical melt resistivity and the bulk resistivity determined by 3D inversion. Vertical arrow shows melt fraction interval compatible with the resistivity model. (c) Relationship between temperature of andesitic magma and melt fraction (Annen et al., 2008) is used to reduce the parameter space (see text). (d) Resulting space of possible solutions. Vertical arrow shows interval of melt fraction estimations compatible with resistivity model and petrophysical constraints.

5.4. Shallow Magma Chamber C2.1

As shown in Figure 14, resistivity values of the C2.1 conductor are compatible with the results of the andesitic magma samples. We therefore attribute the C2.1 conductor, characterized by resistivity values of 1–5 Ωm and described in Section 4.2, to the shallow magma chamber located beneath the Sabancaya volcano.

This body is located beneath the Sabancaya volcano at depths of ≈3–8 km below the surface, with only few seismic events detected inside it (Figures 6 and 9). The range of melt fractions corresponding to the minimum and maximum estimates of the C2.1 body bulk resistivity is shown in Figure 14d and lies in the range between 0.3 and 0.7. Melt resistivity is calculated after Laumonier et al. (2017), melt fraction is calculated using the modified Archie's law (Equation 6), with connectivity exponent chosen as m = 1 (well-connected conductive phase). Because of the ongoing eruptive process of the Sabancaya volcano, and taken into account the absence of seismicity in the C2.1 body, we expect the average melt fraction to be above the eruptible threshold. The relationship between the temperature of magma and its melt content (Annen et al., 2008) was considered to eliminate thermodynamically impossible combinations of these interconnected parameters in the figure.

In this case the resistivity values do not provide any additional constraints but show good agreement between the resistivity model and petrological results.

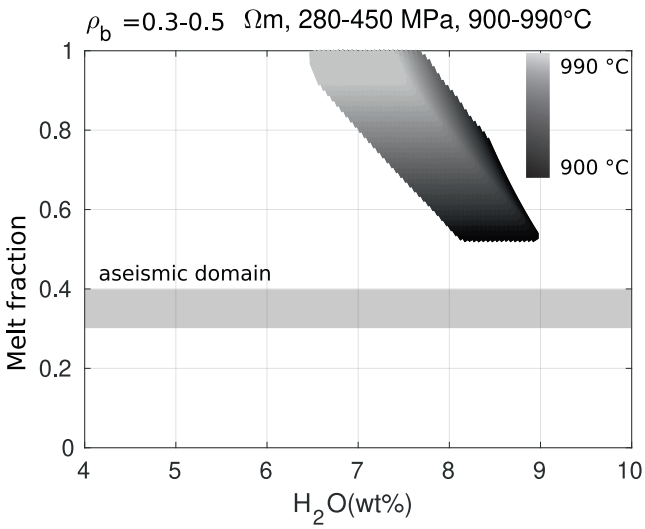

Figure 15. Similar reasoning as in previous Figure applied to estimate the possible range of melt fractions for the resistivity of the deep magma C3 (under assumption of andesitic melt composition). The possible range of melt fractions is situated in the brittle domain below the eruptible critical value (horizontal line).

5.5. Deep Magma Reservoir C3

Figure 15 illustrates similar reasoning for the deep magma reservoir C3, assuming andesitic magma composition. The deep magma reservoir C3 (0.3–0.5 Ωm) is located beneath the Hualca-Hualca volcano at ≈11 − 18 km below the surface. The geothermometers estimate the temperature corresponding to this reservoir between 900 and 1000°C (Gerbe & Thouret, 2004).

Considering the relationship between the temperature of magma and its melt content (Annen et al., 2008), we end up with melt fractions well above eruptible (and aseismic) threshold. We can therefore rule out the bulk resistivity values for which number of seismic events is considerable, that is, <0.6 Ωm (Figure 13b). Assuming an andesitic magma composition, the lower bound of water content in magma is thus ≈6.5 wt% for 100% of melt and ≈9 wt% for melt fraction 0.5 (minimum melt fraction). Noteworthy, if we consider more primitive, for example, basaltic, magma at depth, we would be able to explain the observed resistivities with a lesser magma fraction as basaltic magma has lower resistivity. However, experimental petrology has not evidenced basaltic magma at Sabancaya volcano.

Interpretation of the C3 body as deep magma reservoir agrees well with geodetic and seismic studies. Geodetic studies by Boixart et al. (2020) and MacQueen et al. (2020), performed modeling of the source responsible for the surface deformation area, and determined its location at a depth between 12 and 15 km beneath the Hualca-Hualca volcano. This location corresponds well to the location of the C3 body.

Machacca et al. (2023) documented the occurrence of repetitive earthquakes at distances of 10–20 km northeast of Sabancaya. The authors suggest that these earthquakes are caused by pore pressure wave propagation in the hydrothermal system, which would lead to the reactivation of distant faults. Our results open the possibility that an accumulation of magma in the deep reservoir C3 was the source of pressure that generated seismicity along distant faults in this region as shown in Figures 9b and 10.

5.6. Magmatic Fluids C2.2 and C2.3

The C2.2 conductor is located under the Huambo-Cabanaconde fault system, 16 km northwest of the Sabancaya volcano. Its origin could be associated with earlier intrusions of remnant ultra-saline magmatic fluids, emplaced during the volcanic unrest stage of Sabancaya (from February–July 2013). They in turn would have generated surface deformation (July 2013) and fault activation, causing seismic swarms in July 2013 (Jay et al., 2015; Machacca et al., 2023; Tavera et al., 2013).

The C2.2 body has the bulk resistivity value of 0.1 Ωm. Figure S3 in Supporting Information S1 shows examples of bulk resistivity computations considering three fluid conductivities (10, 30 and 100 S/m) as function of fluid pore fraction (porosity) according to the modified Archie's law Section 5.3. The minimal fluid conductivity that can explain observed bulk resistivity at less than 100% of porosity/melt fraction is ≈30 S/m (Figure S4 in Supporting Information S1). Referring to Jenkins et al. (2023), their Figure 5, where melt conductivities are presented for andesitic, rhyolitic, and basaltic magmas, we conclude that such a high fluid conductivity is not compatible with a magma reservoir. Therefore, we interpret the C.2. body as a deep reservoir rich in ultra-saline brines (Jenkins et al., 2023), which may foster ore-forming conditions.

Concerning C2.3 body, its resistivity is similar to that of C2.2, and therefore it could be interpreted similarly. However, the MT site coverage is limited here and there is no evidence of the recent hydrothermal activity or seismicity. It is therefore difficult to conclude if this body represents an active or an extinct hydrothermal system.

5.7. Shallow Hydrothermal System C1

The shallow conductor C1 (1–10 Ωm) is probably associated with the hydrothermal system of the Ampato-Sabancaya volcanic complex. It follows the topography under the three volcanoes (Ampato, Sabancaya, and

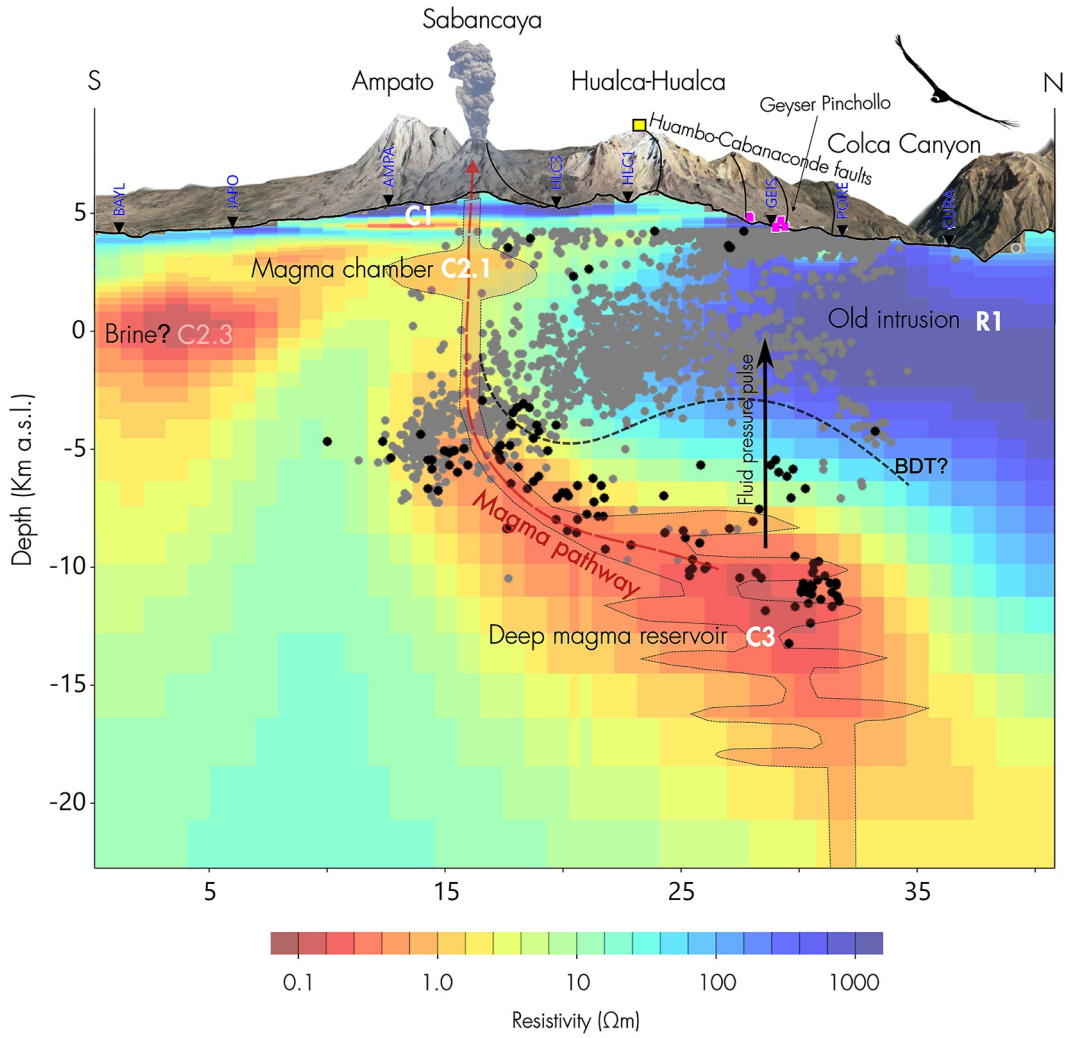

Figure 16. General model proposed for the Sabancaya volcano to explain the resistive structures found by the magnetotelluric method (condor not to scale). The dashed line represents the ductile-brittle transition zone (BDT). The dashed red line represents the path where magmatic fluids would ascend from the deep magmatic reservoir into the magma chamber. Black inverted triangles indicate magnetotelluric sounding site stations, while magenta symbols represent geothermal manifestations. The yellow square marks the maximum inflation point between 2013 and 2019. The black and gray points represent pre- and co-eruptive seismicity, respectively. The vertical black arrow represents fluid movement caused by the pressure gradients originating from magma accumulation (White & McCausland, 2016).

Hualca-Hualca). Preliminary studies using Self-Potential data provide evidence of the existence of an active shallow hydrothermal system below the Ampato and Sabancaya volcanoes (Alvarez, 2017; Puma et al., 2018), which is also confirmed by our current magnetotelluric study. Furthermore, the analysis of the Pinchollo and Puye-Puye thermal springs, rich in sulfates, suggest the hydrothermal system extending to the Hualca-Hualca volcano (Tyc et al., 2022). According to our model, the shallow conductor (C1) would be fed by magmatic fluids (magmatic gases, water, steam, among others) coming from intermediate magmatic zones (C2.1). Machacca et al. (2023) suggest that the progressive heating of the hydrothermal system (C1) by the magmatic gases would cause an increase in pore pressure, which in turn would trigger near-surface earthquakes (1.8–3.5 km deep) during the co-eruptive stage. These events are grouped to the northeast of the Hualca-Hualca volcano (Figures 6 and 9). The origin of the two seismic clusters located on the Sepina fault seems to involve a tectonic component (see Figure 10).

5.8. Conceptual Model

The resistivity profile in the SW-NE direction (Figure 10) and the model proposed (Figure 16) show a potential path that deep magmatic fluids could be taking during their ascent toward shallower areas, reinforcing the view of the studies of Boixart et al. (2020) and MacQueen et al. (2020). Likely, the molten material from the deep magmatic chamber (C3) would supply magmatic fluids to intermediate zones (C2.1, C2.2, and C2.3). Beneath the Sabancaya and Hualca-Hualca volcanoes, magmatic fluids ascending to the surface would generate intense localized seismic activity between ≈5 and 10 km depth; subsequently, they would be temporarily stored in the shallow magmatic chamber (C2.1) before being expelled to the surface through the Sabancaya volcano conduit during volcanic explosions.

6. Conclusions

Plumbing system beneath the Ampato–Sabancaya Volcanic Complex and Hualca-Hualca Volcano has been studied by combining broad band magnetotelluric (MT) imaging with complementary information such as: petrological results, characterization of fault system, various hydrothermal manifestations on the surface, deformation, and seismicity distribution.

The 3D model of electrical resistivity shows strong resistivity contrasts above sea level and generally low resistivity at depth. Co-eruptive seismicity at depths typical for magma feeding systems (<4 km b.s.l.) occurs in an environment characterized by exceptionally low resistivity: 15% of seismic events correspond to the model cells with resistivity lower than 1 Ωm, and 95% of seismic energy is released in the volume characterized by resistivity <10 Ωm.

The model identifies conductive zones referred to (C1, C2.1-C2.3, and C3) as well as two resistive zones (R1 and R2).

The deep magma reservoir is imaged as an electrical conductor C3 with resistivity <0.5 Ωm, at a depth of 11–18 km depth below the Hualca-Hualca volcano, in good agreement with the deformation model of MacQueen et al. (2020). Assuming andesitic magma, melt fractions well above 50% and water content <6.5 wt% are required to explain the observed resistivity. In view of the considerable depth of this reservoir, the hypothesis of more primitive magma composition also seems likely, despite observations of basaltic magma at the surface were not found.

Our model images a lateral pathway from the deep magma reservoir to the C2.1 body located directly below the Sabancaya volcano. The pathway gets around an ancient intrusion (imaged as a resistive body R1), which likely is an obstacle for vertical ascent of magma. We interpret the aseismic C2.1 body with resistivity 2–4 Ωm located at depth of 3–8 km below the Sabancaya volcano, as a shallow magma chamber. Its resistivity and depth, analyzed with petrological constraints, suggest andesitic magma composition with 4–6 wt% of water, and magma fraction of 40%–70%. Magma, injected from the deep reservoir C3, may accumulate temporarily in this body, to be later expelled to the surface through the Sabancaya volcanic conduit by explosions.

One more conductive feature, the C2.2 body, is located in the Huambo-Cabanaconde fault system at depths 2–10 km about 20 km northwest from the Sabancaya volcano. Its resistivity is too low to be explained by the presence of magma. More likely, this body is saturated with ultra-saline brines exsolved from the deep magma reservoir C3 located below it. The latest unrest of Sabancaya in 2013 started with seismicity on the Huambo-Cabanaconde fault system, with hypocenters located clustered between the deep magma reservoir C3 and the C2.2 body. In our interpretation, these seismic events, triggered by fresh magma injection, created a new pathway for exsolved fluids, which replenished the C2.2 body. Moreover, pressurization that resulted from degassing of magma, may have caused the weakening and activation of faults in its general surroundings, within the resistive zones (R1 and R2), triggering intense seismic activity, mostly located to the northwest, north, and northeast at 6–12 km depth below sea level (see also the discussion in MacQueen et al., 2020).

At shallow depth, conductor C1 (1–10 Ωm) is associated with the active hydrothermal system shared by the Sabancaya-Ampato volcanoes and extends horizontally to the Hualca-Hualca at a depth of ≈1–2 km beneath the surface. This interpretation is supported by hydrothermal manifestations: Pinchollo and Puye-Puye thermal springs, geysers, and shallow earthquakes (hypocenter depths range from 4.2 to 2.5 km a.s.l.) located northeast and north of Sabancaya volcano, were likely triggered by pressurization due to magmatic degassing and heating.

Conflict of Interest

The authors declare no conflicts of interest relevant to this study.

Data Availability Statement

This study applied the well known and freely available ModEM code found at (Kelbert et al., 2025). Minor source code modifications for this code, as well as python scripts and modules related to this study the are part of the open source collection Py4MTX (Rath & Byrdina, 2025). The data and software versions used for this publication are available at (Byrdina & Torres, 2025).

Acknowledgments
The project was developed within the framework of the agreement between the Geophysical Institute of Peru (https://www.gob.pe/igp) and the Institute for Dev elopment Research (https://ird.fr/peru). The magnetotelluric data acquisition conducted in November and December 2022 was funded by IRD, IGP, ISTerre, and the "Tellus Program of CNRS-INSU." We thank Jean-Luc Got for his good scientific and practical advice, encouragement, help with equipment, and interesting discussions.The calculations presented in this paper were performed using the GRICAD infrastructure (https://gricad.univ-grenoble-alpes.fr), with the support of the Grenoble and Chambéry research communities. José Luis Torres is funded by the French-Peruvian doctoral school in Engineering Sciences and Geosciences (EDFPCIG, Rectoral Resolutions No. 504/2024), by the National Program for Scientific Research and Advanced Studies of Peru (CONCYTEC-PROCIENCIA) under the framework of the contest "Undergraduate and Postgraduate Thesis in Science, Technology, and Technological Innovation—Contest E073-2024-01" (contract number PE501091976-2024). We also thank the Institute of Radio Astronomy and the Department of Engineering of the Pontifical Catholic University of Peru (INRAS-PUCP) for providing laboratory space and access to office computers, which greatly facilitated data processing and analysis. We thank Hugo Sanchez-Reyes for fruitful discussions and advice of calculating seismic moment for Figure 13. Thanks to Darcy Cordell, whose scripts (Cordell, 2022) we used to produce Figure 14. We also are grateful to Anna Kelbert, Gary Egbert, and particularly Naser Meqbel for making ModEM and 3D-Grid available to us, and for their continuous support. The colleagues from IRD Lima provided invaluable administrative and logistical help. Finally, we thank Cedar Hanneson and Pierre Wawrzyniak for their thoughtful reviews, which improved this paper considerably. Open access publication funding provided by COUPERIN CY26.

References

Aizawa, K. (2016). Recent progress in electromagnetic observations for volcanology. *Bulletin of the Volcanological Society of Japan*, *61*(2), 345–365. https://doi.org/10.18940/kazan.61.2_345

Alvarez, Y. (2017). *Estudio estructural del Sistema Hidrotermal de los volcanes Sabancaya y Hualca-Hualca mediante el método de potencial espontáneo (Doctoral dissertation)*. Universidad Nacional de San Agustín de Arequipa. Retrieved from http://hdl.handle.net/20.500.12816/4833

Amitrano, D. (2003). Seismicity and brittle-ductile transition: Evidence of the b-value pressure dependence. *Journal of Geophysical Research*, *108*(B1), 2044. https://doi.org/10.1029/2001JB000680

Annen, C., Pichavant, M., Bachmann, O., & Burgisser, A. (2008). Conditions for the growth of a long-lived shallow crustal magma chamber below Mount Pelee volcano (Martinique, Lesser Antilles Arc). *Journal of Geophysical Research*, *113*(B7), B07209. https://doi.org/10.1029/2007JB005049

Antayhua, Y., Tavera, H., Bernal, Y., Palza, H., & Aguilar, V. (2002). Localización hipocentral y características de la fuente de los sismos de Maca (1991), Sepina (1992) y Cabanaconde (1998) región del volcán Sabancaya (Arequipa). *Boletin de la Sociedad Geologica del Peru*, *93*, 63–72.

Arzi, A. A. (1978). Critical phenomena in the rheology of partially melted rocks. *Tectonophysics*, *44*(1–4), 173–184. https://doi.org/10.1016/0040-1951(78)90069-0

Becerril, L., Galindo, I., Gudmundsson, A., & Morales, J. M. (2013). Depth of origin of magma in eruptions. *Scientific Reports*, *3*(1), 2762. https://doi.org/10.1038/srep02762

Beck, S. L., Zandt, G., Myers, S. C., Wallace, T. C., Silver, P. G., & Drake, L. (1996). Crustal-thickness variations in the central Andes. *Geology*, *24*(5), 407–410. https://doi.org/10.1130/0091-7613(1996)024⟨0407:CTVITC⟩2.3.CO;2

Becken, M., Ritter, O., Bedrosian, P. A., & Weckmann, U. (2011). Correlation between deep fluids, tremor and creep along the central San Andreas fault. *Nature*, *480*(7375), 87–90. https://doi.org/10.1038/nature10609

Bennington, N., Schultz, A., Bedrosian, P., Bowles-Martinez, E., Lynn, K., Stelten, M., et al. (2025). The progression of basaltic–rhyolitic melt storage at Yellowstone Caldera. *Nature*, *637*(8044), 97–102. https://doi.org/10.1038/s41586-024-08286-z

Blundy, J., Afanasyev, A., Tattitch, B., Sparks, S., Melnik, O., Utkin, I., & Rust, A. (2021). The economic potential of metalliferous sub-volcanic brines. *Royal Society Open Science*, *8*(6), 202192. https://doi.org/10.1098/rsos.202192

Boixart, G., Cruz, L. F., Miranda Cruz, R., Euillades, P. A., Euillades, L. D., & Battaglia, M. (2020). Source model for Sabancaya volcano constrained by DInSAR and GNSS surface deformation observation. *Remote Sensing*, *12*(11), 1852. https://doi.org/10.3390/rs12111852

Booker, J. R. (2014). The magnetotelluric phase tensor: A critical review. *Surveys in Geophysics*, *35*(1), 7–40. https://doi.org/10.1007/s10712-013-9234-2

Burchardt, S. (2018). *Volcanic and igneous plumbing systems: Understanding magma transport, storage, and evolution in the Earth's crust*. Elsevier.

Byrdina, S., & Torres, J. (2025). Data for submitted manuscript to JGR Solid Earth [Data]. *Zenodo*. https://doi.org/10.5281/zenodo.15210885

Cagniard, L. (1953). Basic theory of the magnetotelluric method of geophysical prospecting. *Geophysics*, *18*(3), 605–635. https://doi.org/10.1190/1.1437915

Caldwell, T. G., Bibby, H. M., & Brown, C. (2004). The magnetotelluric phase tensor. *Geophysical Journal International*, *158*(2), 457–469. https://doi.org/10.1111/j.1365-246x.2004.02281.x

Centeno, R., Machacca, R., Vargas, K., Alvarez, Y., Anccasi, R., Antayhua, Y., et al. (2025). *Actividad eruptiva reciente del volcán Sabancaya: De la calma aparente a la reactivación explosiva de septiembre de 2025 (Informe Técnico N° 027-2025/IGP Ciencias de la Tierra Sólida)*. Instituto Geofísico del Perú. Retrieved from http://hdl.handle.net/20.500.12816/5761

Chaussard, E., & Amelung, F. (2014). Regional controls on magma ascent and storage in volcanic arcs. *Geochemistry, Geophysics, Geosystems*, *15*(4), 1407–1418. https://doi.org/10.1002/2013gc005216

Chave, A. D., & Jones, A. G. (2012). *The magnetotelluric method: Theory and practice*. Cambridge University Press.

Comeau, M. J., Unsworth, M. J., & Cordell, D. (2016). New constraints on the magma distribution and composition beneath Volcan Uturuncu and the southern Bolivian Altiplano from magnetotelluric data. *Geosphere*, *12*(5), 1391–1421. https://doi.org/10.1130/GES01277.1

Cordell, D. (2022). MT1D_DetectMagma [Software]. *Zenodo*. https://doi.org/10.5281/zenodo.5838708

Cordell, D., Naif, S., Troch, J., & Huber, C. (2022). Constraining magma reservoir conditions by integrating thermodynamic petrological models and bulk resistivity from magnetotellurics. *Geochemistry, Geophysics, Geosystems*, *23*(9), e2022GC010455. https://doi.org/10.1029/2022GC010455

Cordell, D., Unsworth, M. J., & Diaz, D. (2018). Imaging the Laguna del Maule Volcanic Field, central Chile using magnetotellurics: Evidence for crustal melt regions laterally-offset from surface vents and lava flows. *Earth and Planetary Science Letters*, *488*, 168–180. https://doi.org/10.1016/j.epsl.2018.01.007

Díaz, D., Zúñiga, F., & Castruccio, A. (2020). The interaction between active crustal faults and volcanism: A case study of the Liquiñe-Ofqui Fault Zone and Osorno volcano, southern Andes, using magnetotellurics. *Journal of Volcanology and Geothermal Research*, *393*, 106806.

Dmitriev, V. I., & Berdichevsky, M. N. (1979). The fundamental model of magnetotelluric sounding. *Proceedings of the IEEE*, *79*(7), 1034–1044. https://doi.org/10.1109/proc.1979.11386

Dong, Z., Xiao, Q., Deng, Y., Han, B., Tang, J., Wang, L., & Wang, J. (2023). Preliminary magnetotelluric investigation of crustal magma plumbing system beneath the Wulanhada volcanic field, northern China: Implications for the Magma reservoir and pathway. *Journal of Volcanology and Geothermal Research*, *443*, 107938. https://doi.org/10.1016/j.jvolgeores.2023.107938

Edmonds, M., & Woods, A. W. (2018). Exsolved volatiles in magma reservoirs. *Journal of Volcanology and Geothermal Research*, *368*, 13–30. https://doi.org/10.1016/j.jvolgeores.2018.10.018

Egbert, G. D., & Kelbert, A. (2012). Computational recipes for electromagnetic inverse problems. *Geophysical Journal International*, *189*(1), 251–267. https://doi.org/10.1111/j.1365-246X.2011.05347.x

Gerbe, M.-C., & Thouret, J.-C. (2004). Role of magma mixing in the petrogenesis of tephra erupted during the 1990–98 explosive activity of Nevado Sabancaya, southern Peru. *Bulletin of Volcanology*, *66*(6), 541–561. https://doi.org/10.1007/s00445-004-0340-3

Glover, P. W. J., Hole, M. J., & Pous, J. (2000). A modified Archie's Law for two conducting phases. *Earth and Planetary Science Letters*, *180*(3–4), 369–383. https://doi.org/10.1016/S0012-821X(00)00168-0

Guillande, R., & Throuret, J. C. (1992). L'activite eruptive actuelle du Volcan Nevado Sabancaya (Sud du Pérou) et lévaluation des menages et des risques: Geologie, cartographie et imagerie satellitaire. In *L'activite eruptive actuelle du volcan nevado sabancaya (sud du pérou) et lévaluation des menages et des risques: Geologie, cartographie et imagerie satellitaire* (p. 132). Geosciences Consultants.

Hanneson, C., & Unsworth, M. J. (2023). Regional-scale resistivity structure of the middle and lower crust and uppermost mantle beneath the southeastern Canadian Cordillera and insights into its causes. *Geophysical Journal International*, *234*(3), ggad183–2052. https://doi.org/10.1093/gji/ggad183

Heise, W., Bannister, S., Williams, C., McGavin, P., Caldwell, T., Bertrand, E., et al. (2024). Magmatic priming of a phreatic eruption sequence: The 2012 Te Maari eruptions at Mt Tongariro (New Zealand) imaged by magnetotellurics and seismicity. *Geophysical Journal International*, *236*(3), 1848–1862. https://doi.org/10.1093/gji/ggae022

Hering, P. (2019). *Advances in magnetotelluric data processing, interpretation and inversion, illustrated by a three-dimensional resistivity model of the Ceboruco Volcano (doctoral dissertation)*. Fachbereich Geowissenschaften/Geographie, Johann Wolfgang Goethe-Universität, Frankfurt am Main. Retrieved from http://meas.uni-frankfurt.de/83788576/PhDThesis_Philip_final.pdf

Hogg, C., Kiyan, D., Rath, V., Junge, A., Hering, P., Castro, C., et al. (2024). Three-dimensional interpretation of magnetotelluric data at Fogo Volcano, Azores Islands. *Journal of Volcanology and Geothermal Research*, *455*, 108183. https://doi.org/10.1016/j.jvolgeores.2024.108183

Huamán, D. (1995). *Métodos y aplicaciones de las imágenes de satélite en la cartografía geológica: El caso del seguimiento y evolución de la amenaza volcánica del Sabancaya (región del Colca, Arequipa) (Unpublished doctoral dissertation)*. Universidad Nacional de San Agustín Arequipa, Peru.

Huaman-Rodrigo, D., Chorowicz, J., Guillande, R., Antallaca, A., Caceres, R., & Aguilar, A. (1993). Remote Sensing contribution on seismo-tectonic hazard in a volcanic active area (Nevado Sabancaya, southern Peru). In *2nd ISAG* (pp. 373–376).

Jay, J. A., Delgado, F. J., Torres, J. L., Pritchard, M. E., Macedo, O., & Aguilar, V. (2015). Deformation and seismicity near Sabancaya volcano, southern Peru, from 2002 to 2015. *Geophysical Research Letters*, *42*(8), 2780–2788. https://doi.org/10.1002/2015gl063589

Jenkins, A. P., Rust, A. C., Blundy, J., & Biggs, J. (2023). Magnetotelluric investigations at Andean volcanoes: Partial melt or saline magmatic fluids? *Journal of Volcanology and Geothermal Research*, *440*, 107852. https://doi.org/10.1016/j.jvolgeores.2023.107852

Kelbert, A., Hao, D., & Curry, M. (2025). ModEM [Software]. *Zenodo*. Retrieved from https://zenodo.org/records/17229565

Kelbert, A., Meqbel, N., Egbert, G. D., & Tandon, K. (2014). ModEM: A modular system for inversion of electromagnetic geophysical data. *Computers & Geosciences*, *66*, 40–53. https://doi.org/10.1016/j.cageo.2014.01.010

Kirkby, A. L., Zhang, F., Peacock, J., Hassan, R., & Duan, J. (2019). The MTPy software package for magnetotelluric data analysis and visualisation. *Journal of Open Source Software*, *4*(37), 1358. https://doi.org/10.21105/joss.01358

Kissling, E., Ellsworth, W., Eberhart-Phillips, D., & Kradolfer, U. (1994). Initial reference models in local earthquake tomography. *Journal of Geophysical Research*, *99*(B10), 19635–19646. https://doi.org/10.1029/93jb03138

Kissling, E., Kradolfer, U., & Maurer, H. (1995). *Program VELEST user's guide-short introduction* (Vol. 22). Institute of Geophysics, ETH Zurich.

Laumonier, M., Gaillard, F., Muir, D., Blundy, J., & Unsworth, M. (2017). Giant magmatic water reservoirs at mid-crustal depth inferred from electrical conductivity and the growth of the continental crust. *Earth and Planetary Science Letters*, *457*, 173–180. https://doi.org/10.1016/j.epsl.2016.10.023

Liu, L., & Hasterok, D. (2016). High-resolution lithosphere viscosity and dynamics revealed by magnetotelluric imaging. *Science*, *353*(6307), 1515–1519. https://doi.org/10.1126/science.aaf6542

Lomax, A., Virieux, J., Volant, P., & Berge-Thierry, C. (2000). Probabilistic earthquake location in 3d and layered models. In C. H. Thurber & N. Rabinowitz (Eds.), *Advances in Seismic Event Location* (pp. 101–134). Springer Netherlands. https://doi.org/10.1007/978-94-015-9536-0_5

Machacca, R., Lesage, P., Tavera, H., Pesicek, J. D., Caudron, C., Torres, J. L., et al. (2023). The 2013–2020 seismic activity at Sabancaya Volcano (Peru): Long lasting unrest and eruption. *Journal of Volcanology and Geothermal Research*, *435*, 107767. https://doi.org/10.1016/j.jvolgeores.2023.107767

MacQueen, P., Delgado, F., Reath, K., Pritchard, M. E., Bagnardi, M., Milillo, P., et al. (2020). Volcano-tectonic interactions at Sabancaya volcano, Peru: Eruptions, magmatic inflation, moderate earthquakes, and fault creep. *Journal of Geophysical Research: Solid Earth*, *125*(5), e2019JB019281. https://doi.org/10.1029/2019jb019281

Mering, C., Huaman-Rodrigo, D., Chorowicz, J., Deffontaines, B., & Guillande, R. (1996). New data on the geodynamics of southern Peru from computerized analysis of SPOT and SAR ERS-1 images. *Tectonophysics*, *259*(1–3), 153–169. https://doi.org/10.1016/0040-1951(96)00034-0

Nolasco, R., Tarits, P., Filloux, J., & Chave, A. (1998). Magnetotelluric imaging of the Society Islands hotspot. *Journal of Geophysical Research*, *103*(B12), 287–309. https://doi.org/10.1029/98jb02129

Nur, A., Mavko, G., Dvorkin, J., & Galmudi, D. (1998). Critical porosity: A key to relating physical properties to porosity in rocks. *The Leading Edge*, *17*(3), 357–362. https://doi.org/10.1190/1.1437977

Padilha, A. (1999). Behaviour of magnetotelluric source fields within the equatorial zone. *Earth Planets and Space*, *51*(10), 1119–1125. https://doi.org/10.1186/bf03351585

Padilha, A., Vitorello, I., & Rijo, L. (1997). Effects of the equatorial electrojet on magnetotelluric surveys: Field results from Northwest Brazil. *Geophysical Research Letters*, *24*(1), 89–92. https://doi.org/10.1029/96gl03792

Parker, R. L., & Booker, J. R. (1996). Optimal one-dimensional inversion and bounding of magnetotelluric apparent resistivity and phase measurements. *Physics of the Earth and Planetary Interiors*, *98*(3–4), 269–282. https://doi.org/10.1016/s0031-9201(96)03191-3

Parkinson, W. (1962). The influence of continents and oceans on geomagnetic variations. *Geophysical Journal International*, *6*(4), 441–449. https://doi.org/10.1111/j.1365-246x.1962.tb02992.x

Pavez, M., Schill, E., Held, S., Díaz, D., & Kohl, T. (2020). Visualizing preferential magmatic and geothermal fluid pathways via electric conductivity at Villarrica Volcano, S-Chile. *Journal of Volcanology and Geothermal Research*, *400*, 106913. https://doi.org/10.1016/j.jvolgeores.2020.106913

Peacock, J. R., Mangan, M. T., McPhee, D., & Wannamaker, P. E. (2016). Three-dimensional electrical resistivity model of the hydrothermal system in Long Valley Caldera, California, from magnetotellurics. *Geophysical Research Letters*, *43*(15), 7953–7962. https://doi.org/10.1002/2016gl069263

Puma, N., Macedo Sánchez, O. E., Álvarez, Y., Finizola, A., & Ramos Palomino, D. A. (2018). *Estudio estructural y del sistema hidrotermal de los volcanes Sabancaya y Hualca-Hualca mediante el método de Potencial Espontáneo (Tech. Rep.)*. Instituto Geológico Minero y Metalúrgico (INGEMMET).

Puma, N., & Torres, J. (2020). *Evaluación y análisis de la actividad sísmica en el volcán Sabancaya, periodo 1990-2019 (Tech. Rep.)*. Instituto Geof ísico del Perú.

Rath, V., & Byrdina, S. (2025). Py4MTX: Python tools for MT [Software]. *Zenodo*. https://doi.org/10.5281/zenodo.17296408

Reinsch, T., Dobson, P., Asanuma, H., Huenges, E., Poletto, F., & Sanjuan, B. (2017). Utilizing supercritical geothermal systems: A review of past ventures and ongoing research activities. *Geothermal Energy*, *5*, 1–25. https://doi.org/10.1186/s40517-017-0075-y

Rivera, M., Mariño, J., Samaniego, P., Delgado, R., & Manrique, N. (2016). *Geología y evaluación de peligros del complejo volcánico Ampato-Sabancaya, Arequipa-[Boletín C 61] (Tech. Rep.)*. Instituto Geológico Minero y Metalúrgico (INGEMMET).

Rivera, M., Samaniego, P., Nauret, F., Mariño, J., & Liorzou, C. (2023). Petrological and geochemical constraints on the magmatic evolution at the Ampato-Sabancaya compound volcano (Peru). *Lithos*, *458*, 107364. https://doi.org/10.1016/j.lithos.2023.107364

Rodgers, C. D. (2000). *Inverse methods for atmospheric sounding*. World Scientific.

Samaniego, P., Rivera, M., Manrique, N., Schiavi, F., Nauret, F., Liorzou, C., & Ancellin, M.-A. (2020). Linking magmatic processes and magma chemistry during the post-glacial to recent explosive eruptions of Ubinas volcano (southern Peru). *Journal of Volcanology and Geothermal Research*, *407*, 107095. https://doi.org/10.1016/j.jvolgeores.2020.107095

Samaniego, P., Rivera, M., Marino, J., Guillou, H., Liorzou, C., Zerathe, S., et al. (2016). The eruptive chronology of the Ampato-Sabancaya volcanic complex (southern Peru). *Journal of Volcanology and Geothermal Research*, *323*, 110–128. https://doi.org/10.1016/j.jvolgeores.2016.04.038

Samrock, F., Bachmann, O., & Saar, M. (2021). Integrated magnetotelluric and petrological analysis of felsic magma reservoirs: Insights from Ethiopian rift volcanoes. *Earth and Planetary Science Letters*. https://doi.org/10.31223/X5Q600

Sébrier, M., Mercier, J. L., Mégard, F., Laubacher, G., & Carey-Gailhardis, E. (1985). Quaternary normal and reverse faulting and the state of stress in the central Andes of south Peru. *Tectonics*, *4*, 739–780.

Sebrier, M., & Soler, P. (1991). Tectonics and magmatism in the Peruvian Andes from late Oligocene time to the present. *Geological Society of America Special Paper*, *265*, 259–278.

Siebert, L., Simkin, T., & Kimberly, P. (2011). *Volcanoes of the world*. University of California Press.

Simpson, F., & Bahr, K. (2005). *Practical magnetotellurics*. Cambridge University Press.

Takeda, Y.-T., & Obata, M. (2003). Some comments on the rheologically critical melt percentage. *Journal of Structural Geology*, *25*(5), 813–818. https://doi.org/10.1016/S0191-8141(02)00080-9

Tarantola, A. (2005). *Inverse problem theory and methods for model parameter estimation*. SIAM.

Tavera, H., Guardia Anampa, P. A., Condori Quispe, C., Fernandez, E., & Arredondo García, L. M. (2013). *Sismos de la región del volcán Sabancaya del 22 y 23 de febrero del 2013: aspectos sismológicos (Tech. Rep.)*. Instituto Geofísico del Perú(IGP).

Tavera, H., Guzmán Mendivil, J. L., Velarde Quispe, L., & Cuya Crispin, Á. A. (2016). *Sismo de Ichupampa del 14 de agosto del 2016 (5.3 ML) (Chivay–Arequipa): aspectos sismológicos (Tech. Rep.)*. Instituto Geofísico del Perú(IGP).

Thouret, J.-C., Guillande, R., Huaman, D., Gourgaud, A., Salas, G., & Chorowicz, J. (1994). L'Activite actuelle du Nevado Sabancaya (sud Perou); reconnaissance geologique et satellitaire, evaluation et cartographie des menaces volcaniques. *Bulletin de la Societe Geologique de France*, *165*, 49–63.

Tikhonov, A. (1950). On determining electric characteristics of the deep layers of the earth's crust. *Doklady Akademii Nauk SSSR*, *73*, 295–297.

Torres, J.-L. (2014). *Evaluación de la actividad sismovolcánica asociada a la intranquilidad del volcán Sabancaya, período enero-julio 2013 (Tech. Rep.)*. Universidad Nacional de San Agustín de Arequipa(UNSA).

Tyc, A., Gaidzik, K., Ciesielczuk, J., Masías, P., Paulo, A., Postawa, A., & Żaba, J. (2022). Thermal springs and active fault network of the central Colca River basin, Western Cordillera, Peru. *Journal of Volcanology and Geothermal Research*, *424*, 107513. https://doi.org/10.1016/j.jvolgeores.2022.107513

Vigneresse, J. L., Berbey, P., & Cuney, M. (1996). Rheological transitions during partial melting and crystallization with application to felsic magma segregation and transfer. *Journal of Petrology*, *37*(6), 1579–1600. https://doi.org/10.1093/petrology/37.6.1579

Viljanen, A. (2012). *The Magnetotelluric Method: Theory and Practice*. In A. Chave & A. Jones (Eds.), (pp. 108–131). Cambridge University Press.

Watanabe, N., Mogi, T., Yamaya, Y., Kitamura, K., Asanuma, H., & Tsuchiya, N. (2022). Electrical conductivity of H2O-NaCl fluids under supercritical geothermal conditions and implications for deep conductors observed by the magnetotelluric method. *Geothermics*, *101*, 102361. https://doi.org/10.1016/j.geothermics.2022.102361

Wawrzyniak, P., Gaillard, F., Hautot, S., Andujar, J., Tarits, P., Arbaret, L., et al. (2025). Magnetotelluric evidence for a melt-rich magmatic reservoir beneath Mayotte. *Nature*, *646*(8087), 1122–1128. https://doi.org/10.1038/s41586-025-09625-4

White, R., & McCausland, W. (2016). Volcano-tectonic earthquakes: A new tool for estimating intrusive volumes and forecasting eruptions. *Journal of Volcanology and Geothermal Research*, *309*, 139–155. https://doi.org/10.1016/j.jvolgeores.2015.10.020

Wiese, H. (1962). Geomagnetische Tiefentellurik. Teil II: Die Streichrichtung der Untergrundstrukturen des elektrischen Widerstandes, erschlossen aus geomagnetischen Variationen. *Pure and Applied Geophysics*, *52*(1), 83–103. https://doi.org/10.1007/BF01996002

Erratum

The originally published version of this article omitted acknowledgment of the role of Supervision from coauthor Svetlana Byrdina. The error has been corrected, and this may be considered the authoritative version of record.